






Article

Wavelength Dependence of the Transformation Mechanism of Sulfonamides Using Different LED Light Sources and TiO₂ and ZnO Photocatalysts

Máté Náfrádi ¹, Tünde Alapi ^{1,*}, Luca Farkas ¹, Gábor Bencsik ², Gábor Kozma ³ and Klára Hernádi ⁴

¹ Department of Inorganic and Analytical Chemistry, University of Szeged, Dóm tér 7, H-6720 Szeged, Hungary; nafradim@chem.u-szeged.hu (M.N.); fluca@chem.u-szeged.hu (L.F.)

² Department of Physical Chemistry and Materials Science, University of Szeged, Rerrich Béla tér 1, H-6720 Szeged, Hungary; bencsikg@chem.u-szeged.hu

³ Department of Applied and Environmental Chemistry, University of Szeged, Rerrich Béla tér 1, H-6720 Szeged, Hungary; kozmag@chem.u-szeged.hu

⁴ Institute of Physical Metallurgy, Metal Forming and Nanotechnology, University of Miskolc, C/2-5 Building 209, H-3515 Miskolc-Egyetemvaros, Hungary; femhernadi@uni-miskolc.hu

* Correspondence: alapi@chem.u-szeged.hu

Abstract: The comparison of the efficiency of the commercially available photocatalysts, TiO₂ and ZnO, irradiated with 365 nm and 398 nm light, is presented for the removal of two antibiotics, sulfamethazine (SMT) and sulfamethoxypyridazine (SMP). The •OH formation rate was compared using coumarin, and higher efficiency was proved for TiO₂ than ZnO, while for 1,4-benzoquinone in O₂-free suspensions, the higher contribution of the photogenerated electrons to the conversion was observed for ZnO than TiO₂, especially at 398 nm irradiation. An extremely fast transformation and high quantum yield of SMP in the TiO₂/LED_{398nm} process were observed. The transformation was fast in both O₂ containing and O₂-free suspensions and takes place via desulfonation, while in other cases, mainly hydroxylated products form. The effect of reaction parameters (methanol, dissolved O₂ content, HCO₃⁻ and Cl⁻) confirmed that a quite rarely observed energy transfer between the excited state P25 and SMP might be responsible for this unique behavior. In our opinion, these results highlight that “non-conventional” mechanisms could occur even in the case of the well-known TiO₂ photocatalyst, and the effect of wavelength is also worth investigating.

Keywords: energy transfer; direct charge transfer; matrix effect; sulfonamides



Citation: Náfrádi, M.; Alapi, T.; Farkas, L.; Bencsik, G.; Kozma, G.; Hernádi, K. Wavelength Dependence of the Transformation Mechanism of Sulfonamides Using Different LED Light Sources and TiO₂ and ZnO Photocatalysts. *Materials* **2022**, *15*, 49. <https://doi.org/10.3390/ma15010049>

Academic Editors: Alina Pruna, Klára Hernádi, Zsolt Pap and Tünde Alapi

Received: 4 December 2021

Accepted: 21 December 2021

Published: 22 December 2021

Publisher's Note: MDPI stays neutral with regard to jurisdictional claims in published maps and institutional affiliations.



Copyright: © 2021 by the authors. Licensee MDPI, Basel, Switzerland. This article is an open access article distributed under the terms and conditions of the Creative Commons Attribution (CC BY) license (<https://creativecommons.org/licenses/by/4.0/>).

1. Introduction

The release of antimicrobial agents to the environment causes several environmental, ecological, and public health problems [1,2]. Infection caused by antibiotic-resistant bacteria results in more than 33,000 deaths in Europe. Sulfonamides are among the first synthesized and frequently used antibiotics in human and veterinary medicine and, similar to the other antibiotics, highly contribute to the emergence of antibiotic-resistant bacteria [3]. Existing wastewater treatment plants are not designed to remove micropollutants [4,5]; the raw and treated wastewaters carry significant amount of antibiotic-resistant bacteria. Thus, the application of cost-effective additive water treatment methods is required to eliminate the antibiotics from treated waters completely. Advanced Oxidation Processes (AOPs) offer a solution to remove trace amounts of recalcitrant organic pollutants from wastewater. Among other AOPs, heterogeneous photocatalysis has been applied to remove several sulfonamides, using different photocatalysts and light sources [6–17].

During heterogeneous photocatalysis, a photon with energy higher than the bandgap is absorbed by a semiconductor, forming a photogenerated conduction band electron (e_{CB}^-) and a valence band hole (h_{VB}^+), which react with dissolved organic compounds via direct charge transfer reactions or generate different reactive oxygen species (ROS) [18,19],

of which hydroxyl radical ($\cdot\text{OH}$) has primary importance. The rare examples of photocatalytic reactions induced by prevailing energy transfer have been recently reported in literature by considering the excited solid semiconductor as the energy donor. While electron transfer requires direct contact between the semiconductor and the substrate, mediated contact or a certain distance can favor energy transfer [20]. Nosaka et al. explained the formation of singlet oxygen via double electron transfer in the opposite direction [21], while other authors hypothesized energy transfer, even in the case of surface-modified TiO_2 [22,23]. The enhanced transformation of cyanuric acid [22], the selective oxidization of limonene [24,25], and isomerization of caffeic acid in aqueous TiO_2 suspensions were interpreted by energy transfer mechanism [26]. In the case of “trivial energy transfer,” the quenching of the excited semiconductor can occur by the emission of a photon, and the energy transfer to the species takes place by absorption of the emitted photon. Unlike the trivial mechanism, Förster and Dexter energy transfers are radiationless processes, and their manifestation depends strongly on the distance of the acceptor from the semiconductor [20].

The two most often investigated photocatalysts, TiO_2 and ZnO , have several favorable properties but are mainly active in the UV region. The commercially available TiO_2 photocatalyst, P25, contains two crystal phases: the bandgap of rutile is 3.0 eV, while the anatase phase is 3.2 eV, which is approximately equal to the ZnO bandgap [27–29]. The excellent photocatalytic activity of P25 TiO_2 is often attributed to its mixed crystal phases. Some authors observed individual anatase- and rutile-phase TiO_2 particles without a heterojunction structure [30,31], while others observed a mixture of amorphous TiO_2 with anatase or rutile phase and/or anatase particles covered by a thin overlayer of rutile [32–36]. Ohtani et al. proved the absence of synergetic effect, and found that P25 is a simple mixture of anatase and rutile without any interactions [37,38]. On the contrary, under visible light (>400 nm) irradiation, the superior photocatalytic activity of P25 was originated from the anatase–rutile interparticle contact, which is beneficial to the charge carrier separation and consequently the efficiency [33,36,39,40]. A comprehensive understanding of P25 microstructure should be crucial for designing an efficient TiO_2 -based photocatalyst.

Nowadays, many researchers are involved in synthesizing and characterizing new materials or composite materials based on TiO_2 [41–43] or ZnO [29,44–47], which can be used as effective photocatalysts. However, the use of these new visible light-active photocatalysts often faces a number of problems, such as low quantum efficiency, photocorrosion, or photodissolution, or a high degree of selectivity to remove organic matter [48]. The efficiency of TiO_2 and ZnO as photocatalysts applied for the elimination of organic trace pollutants under UV radiation is not easy to exceed. TiO_2 and ZnO were investigated to transform various sulfonamides [4,15–17,49,50]. Both catalysts were effective; however, the efficiency depended on the chemical structure of sulfonamide, and generally, TiO_2 P25 provided better efficiency than ZnO , especially in the presence of H_2O_2 [16]. Comparing the efficiency of heterogeneous photocatalysis to other AOPs, sulfonamide degradation is highly cost-effective for ozonation, but toxic, ozone resistant intermediates forms, while using TiO_2 or ZnO , the mineralization is also efficient. Several visible light-activated photocatalysts (g- C_3N_4 [10,14], Bi_2O_4 [12], $\text{Bi}_2\text{MoO}_6/\text{Bi}_2\text{WO}_6$ [13], WO_3 [11]; $\text{Ce}_x\text{Zr}_y\text{O}_2$ [7]) were also tested with sulfonamides, with usually lower efficiency compared to TiO_2 and ZnO , although some promising results can also be found. The efficiency of BiOI/BiOCl composite photocatalyst for the degradation of SMP and methyl orange under UV (398 nm) and visible light irradiation was comparable to TiO_2 P25, but highly toxic intermediates were accumulated opposite to the P25, which was efficient for mineralization and toxicity decrease [51]. Besides developing new photocatalysts, using more efficient light sources such as UV or UV/Vis LEDs, and advanced reactor designs may enhance the cost efficiency of the method [19,52,53]. In addition to their many advantages, one of the benefits of LEDs [54–56] is that they emit their photons over a relatively narrow wavelength range to be well adapted to the absorption properties of photocatalysts and provide an opportunity to handle the wavelength-depending effects easily [57–60].

One of the barriers to the practical application of heterogeneous photocatalysis is the adverse effect of the matrix and its parameters on efficiency. Dissolved organic matter and inorganic ions may act as UV filters, radical scavengers or adsorbing on the catalysts' surface can occupy the active sites and reduce efficiency [61–64]. Besides the adverse effects, the adsorption of some ions might result in better charge separation, or their reaction with photogenerated charge carriers results in the formation of less reactive and more selective radicals (e.g., Cl^\bullet , $\text{CO}_3^{\bullet-}$, $\text{SO}_4^{\bullet-}$) than $\bullet\text{OH}$ which could contribute to the transformation of given organic pollutants [61,65–68].

The current research aimed to compare the efficiency of the commercially available photocatalysts, TiO_2 and ZnO , irradiated with two LED light sources; a high power UV-A LED emitting at 365 nm ($\text{LED}_{365\text{nm}}$) and a cheap commercial LED-tape emitting at 398 nm ($\text{LED}_{398\text{nm}}$). The removal of two sulfonamide antibiotics, sulfamethazine (SMT) and sulfamethoxypyridazine (SMP), was investigated in detail and compared based on removal and mineralization rates. The direct detection of reactive species in the case of heterogeneous photocatalysis is rather difficult; however, the knowledge of their formation rate under given circumstances is crucial for the elucidation of degradation mechanism and the assessment of photocatalytic activity. The $\bullet\text{OH}$ formation rates were compared using coumarin (COU) as a model compound. The rate and importance of the direct charge transfer process were compared using 1,4-benzoquinone (1,4-BQ) in O_2 -free suspensions. The formation of organic and inorganic degradation products of sulfonamides and the ecotoxicity of the treated solutions were also investigated. Experiments were performed in real water matrices (tap water and biologically treated wastewater), and the effect of methanol as $\bullet\text{OH}$ scavenger and the most abundant anions (Cl^- , HCO_3^-) of the matrices was also investigated.

2. Materials and Analytical Methods

2.1. Photochemical Experiments

Two photoreactors were used during the photocatalytic experiments. One was equipped with 12 high-power UV—A LED light sources (Vishay, Malvern, PA, USA; VLMU3510-365-130, 0.69 W radiant power at 2.0 W electric power input) emitting at 365 nm ($\text{LED}_{365\text{nm}}$). A laboratory power supply (Axiomet, Malmö, Sweden; AX-3005DBL-3; maximum output 5.0 A/30.0 V) was used to control the electrical power uptake of the light sources (6.6 W). Irradiations were performed in a 200 cm^3 cylindrical glass reactor placed inside the hexagonally arranged LEDs (Figure S1a). The solutions were bubbled with gas from a porous glass filter. Synthetic air or N_2 (99.995%) was used depending on the measurements.

The other photochemical reactor was equipped with commercial UV-LED tapes (LED-master, Szeged, Hungary; 4.6 W electric power input; 60 diodes/m) fixed on the inside of a double-walled, water-cooled reactor ($\text{LED}_{398\text{nm}}$) (Figure S1b). Solutions were irradiated in a 100 cm^3 glass reactor; the suspension was bubbled with synthetic air. The emission spectra of both light sources have been measured using a two-channel fiber-optic AvaSpec-FT2048 CCD spectrometer (Avantes, Netherlands).

Two commercially available photocatalysts were used during the experiments, TiO_2 Aeroxide[®] P25 and ZnO . When not stated otherwise, the concentration of the photocatalyst suspensions was 1.00 g dm^{-3} and 1.0×10^{-4} M solutions of COU, SMT, and SMP and 2.0×10^{-4} M solutions of 1,4-BQ were irradiated. The suspension was stirred and bubbled with air or N_2 for 30 min in the dark; and the measurement was started by turning on the light source. Before analysis, the samples were centrifuged (Dragonlab, Beijing, China, 15,000 RPM) and filtered using syringe filters (FilterBio, FilterBio Nantong, China; PVDF-L; 0.22 μm).

2.2. Analytical Methods

X-ray diffractometry (XRD) measurements were performed with a Rigaku Miniflex II (Rigaku, Tokyo, Japan; $\text{Cu K}\alpha$ radiation source, 3.0–90.0 $2\theta^\circ$ range, with 4.0 $2\theta^\circ \text{ min}^{-1}$ resolution). The specific surface area was determined via N_2 adsorption/desorption

isotherms using a Quantachrome NOVA 2200 analyzer (Quantachrome, Boynton Beach, FL, USA). The pore size distribution was calculated by the BJH method. Diffuse reflectance spectroscopy (DRS) was performed using an Ocean Optics USB4000 detector and Ocean Optics DH-2000 light source (Ocean Optics, Largo, FL, USA). The bandgap energy values of the photocatalysts were evaluated by the Kubelka–Munk approach and the Tauc plot. The elemental composition of the photocatalysts was characterized by energy-dispersive X-ray spectroscopy (Hitachi S-4700 operating at 20 kV, equipped with a “Röntec” Energy Dispersive Spectrometer with a 12 mm working distance, Hitachi, Tokyo, Japan).

The photon flux of the light sources was measured using potassium–ferrioxalate actinometry [69]. 1.0×10^{-2} M Fe^{3+} –oxalate solutions were irradiated, the released Fe^{2+} was measured after complexation with 1,10-phenanthroline. The Fe^{2+} –phenanthroline complex concentration was measured using UV-Vis spectrophotometry (Agilent 8453, Agilent, Santa Clara, CA, USA). During these measurements, the solutions were bubbled with N_2 .

The concentration of COU was determined using UV-Vis spectrophotometry ($\epsilon_{277\text{nm}} = 10,293 \text{ M}^{-1} \text{ cm}^{-1}$). The concentration of the formed 7-HC was measured using fluorescence spectroscopy (Hitachi F-4500, Hitachi, Tokyo, Japan), the excitation and emission wavelengths were set to 345 nm and 455 nm, respectively. The concentration of 1,4-benzoquinone (1,4-BQ), its product, the 1,4-hydroquinone (1,4-H₂Q), SMT, and SMP was determined by LC-DAD (Agilent 1100, Agilent, Santa Clara, CA, USA, column: Lichrosphere 100, RP-18; 5 μm). In the case of 1,4-BQ and 1,4-H₂Q the eluent consisted of 50 v/v% methanol (MeOH) and 50 v/v% water; the flow rate was $1.0 \text{ cm}^3 \text{ min}^{-1}$, the temperature was set to 25 °C. In the case of SMT and SMP the eluent consisted of 30 v/v% MeOH and 70 v/v% formic acid (0.1 v/v%), the flow rate was $1.00 \text{ cm}^3 \text{ min}^{-1}$, the temperature was set to 35 °C. The detection of 1,4-BQ, 1,4-H₂Q, SMT, and SMP was performed at 250 nm, 210 nm, 265 nm, and 261 nm, respectively. The retention time was 3.4 min, 2.7 min, 9.5 min, and 6.1 min. The initial transformation rates of the model compounds (r_0) were determined from the linear part of the kinetic curves (up to 20% transformation). Given that the photon flux of light sources and the volume of a treated solution differ, it is worth comparing the efficiency based on apparent quantum yield, calculated by the following equation:

$$\Phi = \frac{\text{number of photons reaching the reactor volume} \left(\text{mol}_{\text{photon}} \text{ s}^{-1} \text{ dm}^{-3} \right)}{\text{number of transformed or formed molecule in the treated volume} \left(\text{mol} \text{ s}^{-1} \text{ dm}^{-3} \right)}$$

The number of photons reaching the reactor volume was calculated from the photon flux of light LEDs divided by the volume of the actinometric solution. The volume of the actinometric solution was the same as the treated suspension.

The determination of SMT and SMP products was achieved by LC-MS, with an Agilent LC/MSD VL mass spectrometer (Agilent, Santa Clara, CA, USA) coupled to the same HPLC. The measurements were performed using an ESI ion source and a triple quadrupole analyzer in positive mode (3500 V capillary voltage and 60 V fragmentor voltage). The drying gas flow rate was $13.0 \text{ dm}^3 \text{ min}^{-1}$, and its temperature was 350 °C. The scanned mass range was between 50–1000 AMU.

Total Organic Carbon (TOC) concentration was determined using an Analytik Jena N/C 3100 analyzer (Analytik Jena, Jena, Germany). The formation of inorganic ions (NH_4^+ , NO_2^- , NO_3^- , and SO_4^{2-}) was measured using ion chromatography (Shimadzu Prominence LC-20AD, Shodex 5U-YS-50 column for cation detection, and Shodex NI-424 5U for anion detection, (Shimadzu, Kyoto, Japan)). The eluent was 4.0 mM methanesulfonic acid and a mixture of 2.5 mM phthalic acid for cation determination and 2.3 mM aminomethane for anion determination. The flow rate of the mobile phase was $1.0 \text{ cm}^3 \text{ min}^{-1}$.

The performed ecotoxicity tests (LCK480, Hach-Lange GmbH, Berlin, Germany) were based on the bioluminescence inhibition of the luminescent bacteria *Vibrio fischeri*. Formed H_2O_2 was decomposed in the samples by adding catalase enzyme ($0.20 \text{ mg} \text{ dm}^{-3}$) before starting the ecotoxicity tests. The luminescence of the bacteria was measured using a luminometer (Lumistox 300, Hach-Lange GmbH, Berlin, Germany) after 30 min incubation time.

2.3. Chemicals and Solvents Used

Two commercial photocatalysts were used, TiO₂ Aeroxide® P25 (Acros Organics, Geel, Belgium, 99.5%) and ZnO (Sigma Aldrich, St. Louis, MO, USA, 80%). Experiments were also performed using anatase (Aldrich, St. Louis, MO, USA, 99.8%) and rutile (Aldrich, St. Louis, MO, USA, 99.9%) phase TiO₂. The list of chemicals used during experimental work can be found in Table S1. Tap water (Szeged, Hungary) and biologically treated domestic wastewater (Szeged, Hungary) were used as mild water matrices; the matrix parameters are summarized in Table S2.

3. Results and Discussion

3.1. The Characterization of the Light Sources and the Photocatalysts

The photon flux of the light sources was measured using potassium–ferrioxalate actinometry and was similar: $5.52 \times 10^{-6} \text{ mol}_{\text{photon}} \text{ s}^{-1}$ for LED_{365nm} and $4.68 \times 10^{-6} \text{ mol}_{\text{photon}} \text{ s}^{-1}$ for LED_{398nm}. The emission spectra of the LED light sources are shown in Figure 1a.

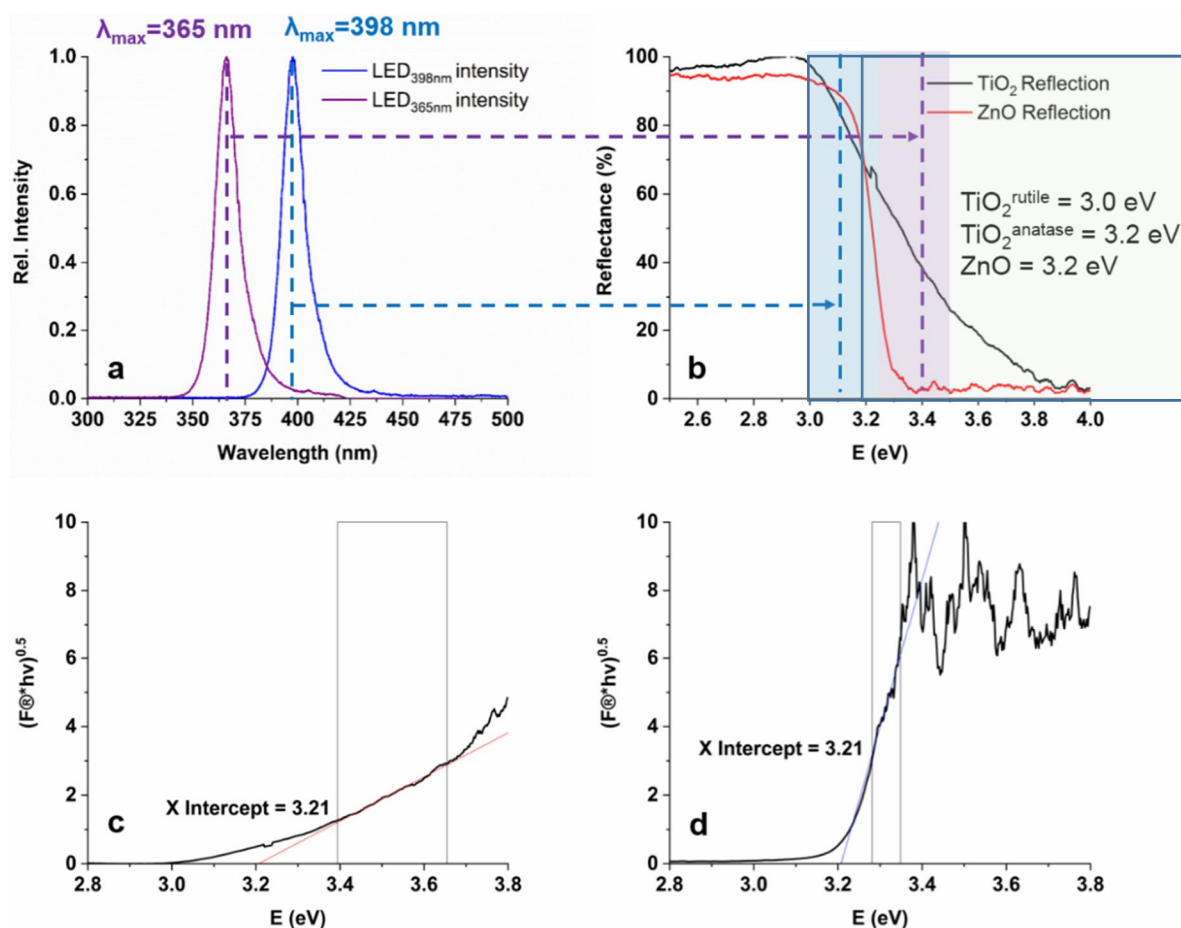


Figure 1. The UV-Vis emission spectra of the LEDs (a), the diffuse reflectance spectra and bandgap energies of TiO₂ and ZnO (b), and the Tauc plot originated from DRS spectra for calculation of band gap energies of TiO₂ (c) and ZnO (d).

Diffuse Reflectance Spectroscopy (DRS) measurements were performed to compare the UV-Vis absorbance and to calculate the bandgap energies of TiO₂ and ZnO (Figure 1b–d). The calculated band gaps were identical, 3.21 eV for TiO₂ and for ZnO. A better light absorption property of ZnO can be observed in the wavelength range emitted by LED_{365nm} (350–400 nm); at 365 nm TiO₂ reflects 40%, while ZnO practically fully absorbs the photons. Within the wavelength range, emitted by LED_{398nm} (380–420 nm) ZnO and TiO₂ show similar absorption properties; no more than 15–20% of the 398 nm photons can be absorbed

(Figure 1b). For TiO₂, the light of LED_{398nm} can excite mainly the rutile phase having 3.0 eV, while LED_{365nm} can cause the charge separation in rutile and anatase TiO₂ and ZnO [36,37].

The specific surface area and pore-size distribution of TiO₂ and ZnO were measured via N₂ adsorption–desorption (Figure 2a). The surface area of TiO₂ was significantly higher (64 m² g^{−1}) than ZnO (13 m² g^{−1}); both measured values are close to the values given by the suppliers. The average primary particle size for Aeroxide P25 TiO₂ is ranges from 10 to 50 nm, largely distributed from 15 to 25 nm [36,70]. For ZnO this value is 50–70 nm [71]. Element analysis of ZnO and TiO₂ has been measured with EDS technology. For both photocatalysts, the stoichiometric amount of cation (49% Zn and 32% Ti for ZnO and TiO₂ respectively) and oxygen (51% for ZnO and 68% for TiO₂) was measured (within the measurement margin of error). Contaminants were not detected. For TiO₂, the XRD pattern is in good agreement with the results reported in the literature; anatase is the dominant crystal phase in the anatase–rutile mixture (Figure 2b) [72,73]. The XRD pattern of ZnO confirmed its pure wurtzite phase (Figure 2b) [44,74].

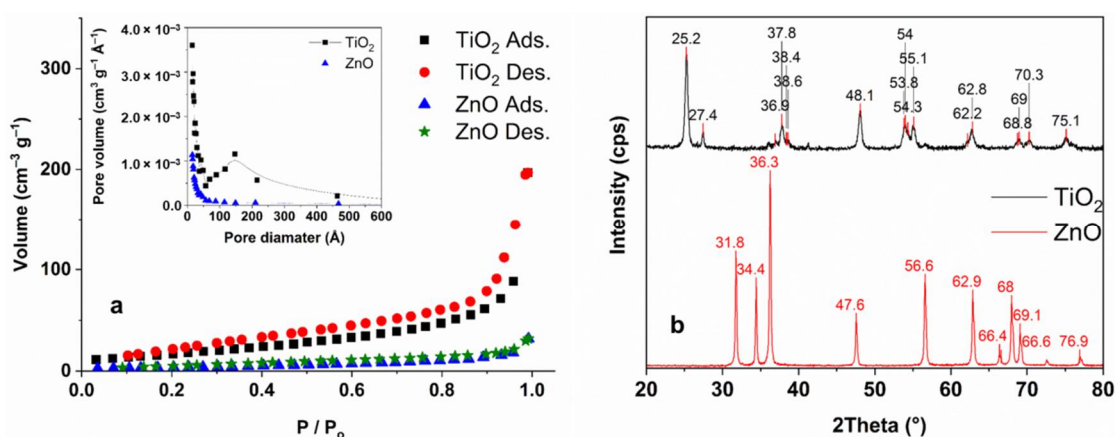


Figure 2. The N₂ adsorption-desorption isotherms (a) with corresponding pore-size distribution according to the BJH model (inset), and the XRD patterns of TiO₂ and ZnO (b).

3.2. Transformation and Mineralization of Sulfonamides

At the given initial concentration (1.0 × 10^{−4} M), the adsorption of both SMT and SMP was negligible (<2%) for both catalysts. The effect of catalyst concentration was studied in the range of 0.25–1.5 g dm^{−3}; the transformation rate does not increase above 1.0 g dm^{−3} TiO₂ and ZnO concentration (Figure 3); thus, 1.0 g dm^{−3} photocatalyst was used for further experiments.

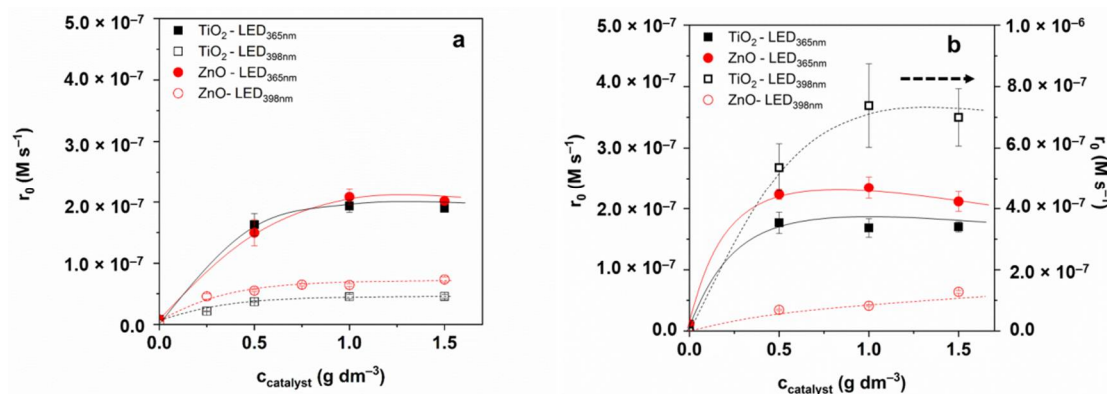


Figure 3. The effect of photocatalyst concentration on the initial transformation rate of SMT (a) and SMP (b).

In the case of SMT, no significant difference was between TiO₂ and ZnO, and LED_{365nm} was more effective than LED_{398nm} (Figure 3a), as was expected. For SMP, using LED_{365nm} ZnO is slightly more efficient than TiO₂. Using TiO₂ and LED_{398nm} an extremely fast

transformation of SMP was observed (Figure 3b), which slows down after 75% decrease of the initial concentration (Figure 4b). Table 1. contains the initial reaction rates and the apparent quantum yields calculated at 1.0 g dm^{-3} photocatalyst dosage. The value determined for SMP $\text{TiO}_2/\text{LED}_{398\text{nm}}$ is about 16 times higher than for SMT $\text{TiO}_2/\text{LED}_{398\text{nm}}$, while for other cases ($\text{TiO}_2/\text{LED}_{365\text{nm}}$, $\text{TiO}_2/\text{LED}_{365\text{nm}}$, $\text{TiO}_2/\text{LED}_{365\text{nm}}$), similar or even lower values were observed for SMP than SMT.

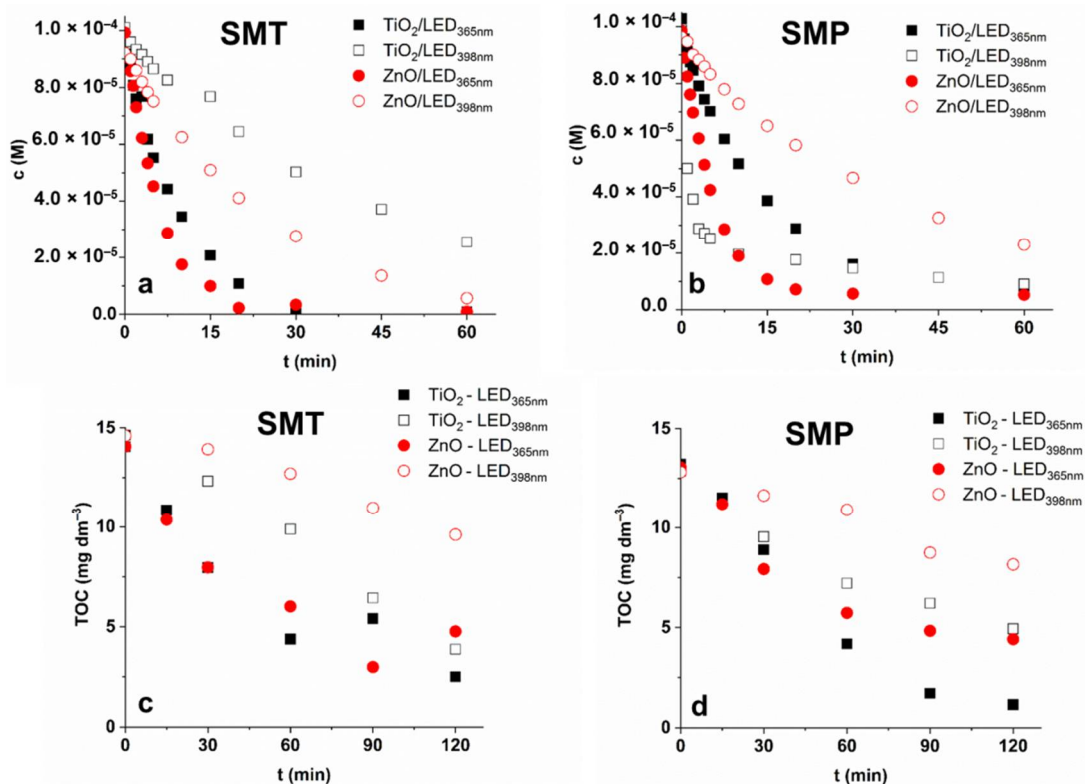


Figure 4. The concentration and TOC content of SMT (a,c) and SMP (b,d) during treatments.

Table 1. The initial transformation rates of SMT and SMP and the apparent quantum efficiencies (Φ) of the related processes.

	TiO_2				ZnO			
	SMT		SMP		SMT		SMP	
	r_0^{SMT} ($\text{mol dm}^{-3} \text{ s}^{-1}$)	Φ^{SMT}	r_0^{SMP} ($\text{mol dm}^{-3} \text{ s}^{-1}$)	Φ^{SMP}	r_0^{SMT} ($\text{mol dm}^{-3} \text{ s}^{-1}$)	Φ^{SMT}	r_0^{SMP} ($\text{mol dm}^{-3} \text{ s}^{-1}$)	Φ^{SMP}
$\text{LED}_{365\text{nm}}$	1.93×10^{-7}	7.0×10^{-3}	1.68×10^{-7}	6.1×10^{-3}	2.08×10^{-7}	7.6×10^{-3}	2.35×10^{-7}	8.5×10^{-3}
$\text{LED}_{398\text{nm}}$	4.53×10^{-8}	9.7×10^{-4}	7.38×10^{-7}	1.6×10^{-2}	6.43×10^{-8}	1.4×10^{-3}	4.12×10^{-8}	8.8×10^{-4}

To interpret the specific behavior of SMP, we first examined and compared the distribution of aromatic intermediates, which are formed and transformed during the first 60 min. of treatment. The proposed structures of the formed products of SMT and SMP are summarized in Figure 5, while product distribution is shown in Figures S2 and S3. For SMT, six stable products were observed on the chromatogram (HPLC-DAD) (Figure S2), and four of them were identified with MS. The SM/3 product ($m/z = 293.2$) resulted by the oxidation of the terminal amino group, while SM/4 ($m/z = 311.0$), SM/5, and SM/6 ($m/z = 295.1$) formed via hydroxylation of the aromatic ring, most probably due to the reaction with $\bullet\text{OH}$ [75,76]. No significant difference was found between the products formed using TiO_2 and ZnO ; however, ZnO produced a higher SM/5 concentration (Figure S2). The distribution of the products does not depend on the wavelength; only their accumulation and decomposition rate was higher using $\text{LED}_{365\text{nm}}$ than $\text{LED}_{398\text{nm}}$.

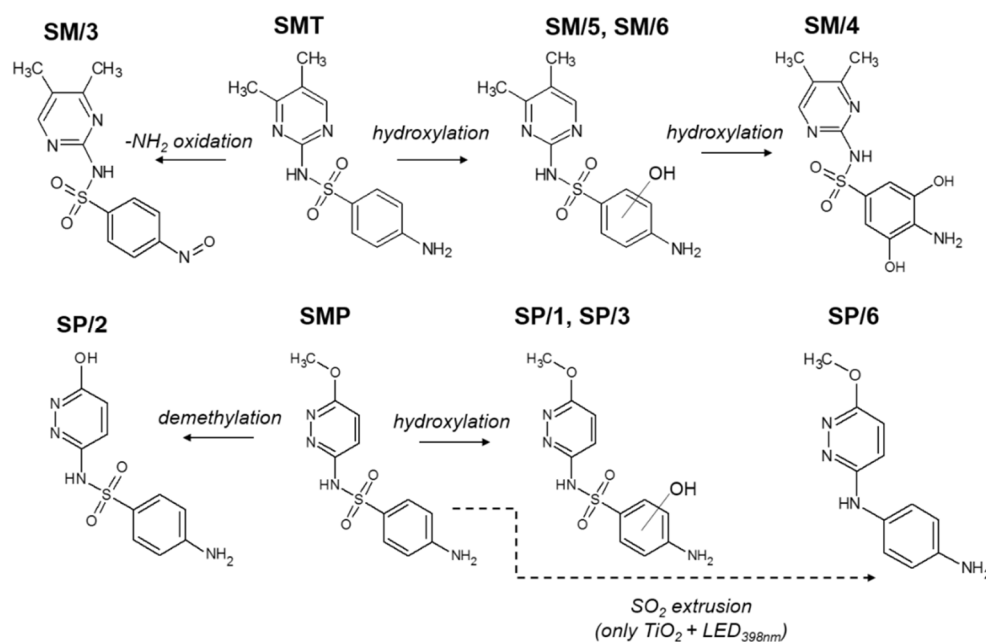


Figure 5. The proposed primary stable products of SMT and SMP transformation during heterogeneous photocatalysis.

In the case of SMP, SP/1 and SP/3 are hydroxylated products ($m/z = 297.1$), while SP/2 ($m/z = 267.0$) is resulted by demethylation [77]. The same products formed with a similar concentration distribution for ZnO using different LEDs. For SMT, the product distribution was similar for TiO₂ and ZnO, while for SMP, it was different; SP/1 and SP/2 formed mainly in the case of ZnO, and SP/4 was observed only for TiO₂ using LED_{365nm}. (Figure S3). However, in the case of TiO₂/LED_{398nm}, not only did the conversion rate of SMP increase drastically but also the intermediates were changed in the case of lower-energy 398 nm radiation: besides the main product SP/6 ($m/z = 217.0$), which forms via -SO₂-extrusion, the formation of hydroxylated products is negligible. The significant change of the primary products in the case of TiO₂/LED_{398nm} process indicates that the reaction mechanism of SMP is different in this case.

The primary product of sulfonamides often forms via desulfonation in both direct and indirect photodegradation processes [78–80]. Boreen et al. attributed the indirect oxidation partly to the interaction with triplet excited-state dissolved organic matters when the -SO₂- extrusion happens due to the electron transfer and not to the energy transfer. The -SO₂- extrusion as the primary transformation way was also reported in a previous work of the authors; the reaction happened selectively, BiOI/BiOCl photocatalysts [51] and direct charge transfer was supposed as the primary transformation process. Ge et al. compared the major conversion pathways for the transformation of different sulfonamides initiated by photolysis, •OH-based, and singlet oxygen and desulfonation was particularly characteristic of photolysis, which includes direct photolysis and photosensitization via triplet excited-state dissolved organic matters [81]. All of these suggest that besides •OH and direct charge transfer, the relative contribution of the reaction with singlet oxygen and direct energy transfer cannot be ignored and, despite their selectivity, can significantly contribute to the conversion of individual sulfonamides.

3.3. Mineralization of Sulfonamides and Ecotoxicity Assays

In the case of ozonation and UV photolysis, the intermediates of sulfonamides often have toxic effects. Moreover, chemicals together produce combination effects that are larger than the effects of the component separately. Thus, the change of ecotoxicity of the treated solution was investigated using *Vibrio fischeri* as a test organism. The 1.0×10^{-4} M concentration SMT and SMP caused a relatively low (<20%) inhibition. For SMT, the toxicity

did not change or even increased slightly due to the formation of toxic products, then slowly decreased as their further transformation progressed (Figure 6a). For SMP, more significant changes were observed; it increased intensively and later decreased, and finally, toxicity lowered below the parent compound in the case of LED_{365nm} (Figure 6b). The ecotoxicity change in the case of LED_{398nm} depends on the photocatalysts: for SMT, the ZnO, while for SMP, the TiO₂ is the more efficient.

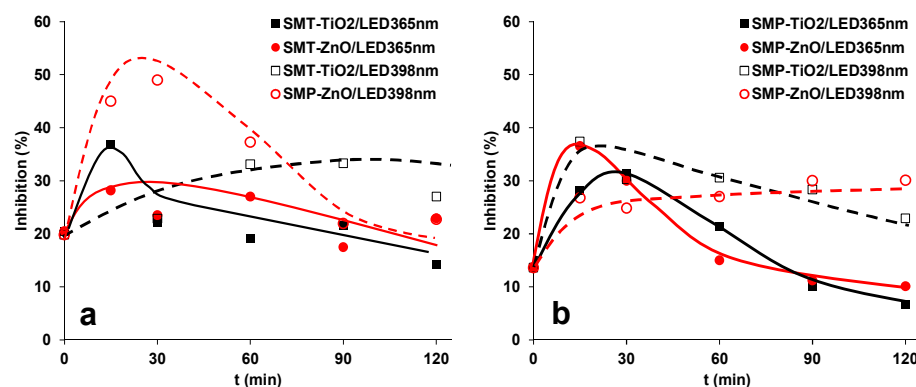


Figure 6. Change of ecotoxicity of the SMT (a) and SMP (b) solutions as a function of treatment time.

The main goal of AOPs is generally not only the transformation but the complete mineralization of pollutants to avoid the accumulation of potentially toxic intermediates. In the case of SMT, both TiO₂ and ZnO irradiated with LED_{365nm} reduced the TOC by ~80%. Using LED_{398nm}, the ZnO is more efficient for SMT transformation than TiO₂, but mineralization is two times faster with TiO₂ and finally (at 120 min) approaches the value measured in the case of LED_{365nm}, while using ZnO/LED_{398nm} no more than 33% TOC was removed (Figure 4c,d).

For SMP, TiO₂ is more efficient (90 and 62% decrease for LED_{365nm} and LED_{398nm}, respectively) than ZnO (66% and 35% decrease for LED_{365nm} and LED_{398nm}, respectively) for TOC decrease in the case of both LEDs (Figure 4c,d), despite that, the SMP transformation rate for ZnO/LED_{365nm} exceeds that for TiO₂/LED_{365nm} (Figure 3b, Table 1). Using TiO₂/LED_{398nm}, not only the transformation rate of SMP was extremely fast (Table 1), but also the mineralization was favorable, especially during the first period of treatment, and finally reached the value measured for ZnO/LED_{365nm}. A plausible explanation of this could be that changes in the mechanism result in more easily oxidizable intermediates and, consequently, increase the mineralization rate. Comparing the mineralization rates, the efficiency change in the same order for both sulfonamides; and TiO₂ shows better mineralization capacity than ZnO. The difference is much better manifested for LED_{398nm} than LED_{365nm}. It confirms that the •OH is the most important reactive species in terms of mineralization.

For SMT, the formation of inorganic ions (NH₄⁺, NO₃⁻, NO₂⁻ and SO₄²⁻) followed the mineralization efficiency: for LED_{365nm}, similar results were obtained with both catalysts, with a slightly faster SO₄²⁻ formation rate for ZnO and an enhanced NH₄⁺ production for TiO₂ (Figures S4 and S5). In the case of LED_{365nm}, 85% of S-content was detected as SO₄²⁻; lower values (44% for TiO₂ and 65% for ZnO) were measured for LED_{398nm}. For LED_{365nm} there was no significant difference between SMT and SMP in terms of inorganic ion formation rate, but it is worth comparing the SO₄²⁻ conversion of SMT and SMP when TiO₂/LED_{398nm} is used. The SO₄²⁻ conversion for SMT at 15 min is negligible, and no more than 25% at 60 min, while these values are 20% and 50% for SMP, confirming the different conversion mechanisms of the two sulfonamides and the importance of desulfonation for SMP, as the first step of transformation. (Figure S5). The SO₄²⁻-formation rate for TiO₂/LED_{398nm}, when -SO₂-extrusion is supposed to be the dominant transformation pathway, is similar to TiO₂/LED_{365nm} and even faster for ZnO/LED_{365nm} (Figure S5). It proves that desulfonation is an important step not only for TiO₂/LED_{398nm}; it can prob-

ably occur directly from the target substances as the first step of the transformation and from the aromatic intermediates.

No more than 30% of the nitrogen content was transformed into NH_4^+ , the NO_3^- conversion was even lower (<14%) (Figures S4 and S5). For both sulfonamides, NO_2^- formation (<6%) was observed only for ZnO, which likely forms via the reduction of NO_3^- by e_{CB}^- , and not favored on TiO_2 surface [82]. NO_2^- could be easily oxidized with $\bullet\text{OH}$ to NO_3^- ($k_{\text{NO}_2^- + \bullet\text{OH}} = 6.0 \times 10^9 \text{ M}^{-1} \text{ s}^{-1}$ [83]), thus its concentration remains low.

To understand the reason for the unique behavior of the SMP, we have investigated the effect of wavelength and photocatalyst on the $\bullet\text{OH}$ formation rate and charge separation efficiency, using COU and 1,4-BQ.

3.4. Transformation of Coumarin—The Comparison of $\bullet\text{OH}$ Formation Efficiency

The reaction of COU with $\bullet\text{OH}$ ($k_{\text{COU} + \bullet\text{OH}} = 6.9 \times 10^9 \text{ M}^{-1} \text{ s}^{-1}$ [84]) results in highly fluorescent 7-hydroxy-coumarin (7-HC) [85,86]; its formation rate is proportional to the $\bullet\text{OH}$ formation rate. The ratio of COU transformation rate and 7-HC formation rate provides further information about the contribution of $\bullet\text{OH}$ to the COU transformation [85,87,88].

The COU adsorption was negligible for both photocatalysts (<1.0%), similar to sulfonamides. The effect of the catalyst dose was determined in previous measurements; the r_0^{COU} reached a maximum value at 1.0 g dm^{-3} in the case of both photocatalysts. In this work, the initial concentration of COU was $1.0 \times 10^{-4} \text{ M}$, and the catalyst dosage was 1.0 g dm^{-3} .

The transformation of COU was slightly faster for ZnO, especially in the case of $\text{LED}_{398\text{nm}}$, while the formation rate of 7-HC was significantly higher for TiO_2 , than for ZnO in both cases (Table 2). The maximum concentration of this hydroxylated product is almost twice for TiO_2 than for ZnO in the case of $\text{LED}_{365\text{nm}}$ and more than three times higher in the case of $\text{LED}_{398\text{nm}}$ (Figure 7a,b). The $r_0^{\text{COU}}/r_0^{7\text{-HC}}$ ratio for TiO_2 (0.027 and 0.041 for $\text{LED}_{365\text{nm}}$ and $\text{LED}_{398\text{nm}}$, respectively) also exceeds the value determined for ZnO (0.019 and 0.025 for $\text{LED}_{365\text{nm}}$ and $\text{LED}_{398\text{nm}}$, respectively). These prove the higher contribution of $\bullet\text{OH}$ to the transformation when TiO_2 is used, mainly when $\text{LED}_{398\text{nm}}$ is applied (Table 2). Most probably, for ZnO the transformation of COU via direct charge transfer processes is favorable due to the higher electron mobility of photogenerated charges [89,90].

Table 2. The initial transformation rates of target substances (r_0^{COU} and $r_0^{1,4\text{-BQ}}$), the initial formation rate of their primary products ($r_0^{7\text{-HC}}$ and $r_0^{1,4\text{-H}_2\text{Q}}$), and the apparent quantum efficiency (Φ) of the related processes.

	TiO_2				ZnO			
	COU \rightarrow 7-HC							
	r_0^{COU} ($\text{mol dm}^{-3} \text{ s}^{-1}$)	Φ^{COU}	$r_0^{7\text{-HC}}$ ($\text{mol dm}^{-3} \text{ s}^{-1}$)	$\Phi^{7\text{-HC}}$	r_0^{COU} ($\text{mol dm}^{-3} \text{ s}^{-1}$)	Φ^{COU}	$r_0^{7\text{-HC}}$ ($\text{mol dm}^{-3} \text{ s}^{-1}$)	$\Phi^{7\text{-HC}}$
$\text{LED}_{365\text{nm}}$	1.53×10^{-7}	5.5×10^{-3}	4.1×10^{-9}	1.5×10^{-4}	1.54×10^{-7}	3.2×10^{-3}	2.88×10^{-9}	0.6×10^{-4}
$\text{LED}_{398\text{nm}}$	3.80×10^{-8}	0.8×10^{-3}	1.5×10^{-9}	0.3×10^{-4}	5.18×10^{-8}	1.1×10^{-3}	1.29×10^{-9}	0.3×10^{-4}
	1,4-BQ \rightarrow 1,4-H ₂ Q							
	r_0^{BQ} ($\text{mol dm}^{-3} \text{ s}^{-1}$)	$\Phi^{1,4\text{-BQ}}$	$r_0^{1,4\text{-H}_2\text{Q}}$ ($\text{mol dm}^{-3} \text{ s}^{-1}$)	$\Phi^{1,4\text{-H}_2\text{Q}}$	r_0^{BQ} ($\text{mol dm}^{-3} \text{ s}^{-1}$)	$\Phi^{1,4\text{-BQ}}$	$r_0^{1,4\text{-H}_2\text{Q}}$ ($\text{mol dm}^{-3} \text{ s}^{-1}$)	$\Phi^{1,4\text{-H}_2\text{Q}}$
$\text{LED}_{365\text{nm}}$	2.78×10^{-6}	1.0×10^{-1}	2.61×10^{-6}	9.5×10^{-2}	3.12×10^{-6}	1.1×10^{-1}	2.47×10^{-6}	8.9×10^{-2}
$\text{LED}_{398\text{nm}}$	8.88×10^{-7}	1.9×10^{-2}	7.61×10^{-7}	1.5×10^{-2}	1.19×10^{-6}	2.6×10^{-2}	8.07×10^{-7}	1.7×10^{-2}

The apparent quantum yield (Φ^{COU}) relates to the COU transformation is higher for TiO_2 than for ZnO (Table 2); opposite that, the light absorption properties of ZnO are more favorable at 365 nm (Figure 1b). When $\text{LED}_{398\text{nm}}$ is used, primarily the rutile phase can be excited due to its lower bandgap. Since the rutile content of TiO_2 is only 15%, the Φ^{COU} is significantly lower at this wavelength than for ZnO (Table 2). Comparing the Φ^{COU} value determined at two different wavelengths was 7 times higher for TiO_2 , but only 3 times higher for ZnO at 365 nm than 398 nm. Similar ratios can be observed for $\Phi^{7\text{-HC}}$ values.

The different wavelengths and photon flux can affect photogenerated charge carriers' formation and recombination rate [91,92], affecting the quantum efficiency of •OH formation.

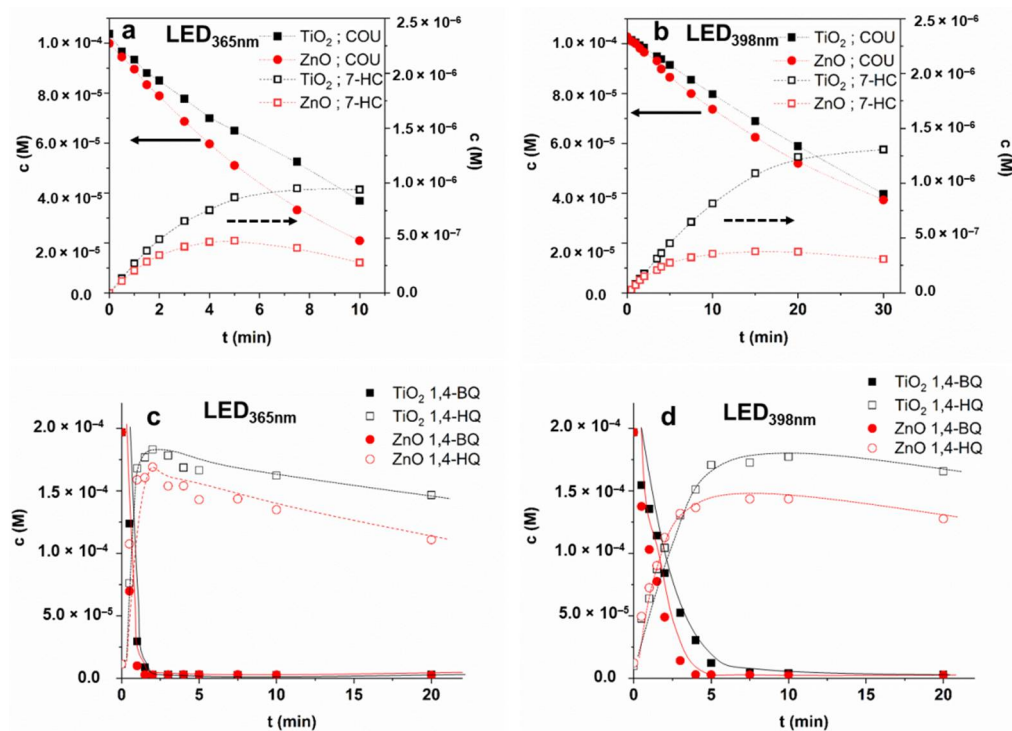
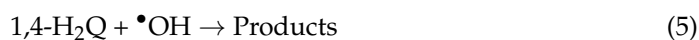
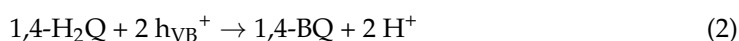
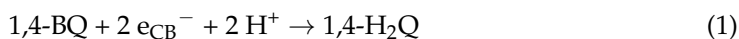


Figure 7. The concentration of COU and 7-HC (a,b) in aerated suspensions and the concentration of 1,4-BQ and 1,4-H₂Q (c,d) in oxygen-free suspensions ((a,c): LED_{365nm}; (b,d): LED_{398nm}).

The efficiency of both photocatalysts was lower at 398 nm, but despite the nearly 80% reflection and the wide bandgaps (3.2 eV), pretty good activities were measured compared to the irradiation at 365 nm. It is probably due to the presence of rutile for TiO₂ and the heterojunction between the rutile and anatase phases. The results on COU conversion confirmed that •OH formation is much more efficient for TiO₂ than for ZnO, and that wavelength also has a significant effect on •OH formation efficiency but does not explain the behavior of SMP.

3.5. Transformation of 1,4-BQ—The Comparison of Charge Separation Efficiency

Besides •OH formation efficiency, the possibility of direct charge transfer and efficiency of e_{CB}⁻ was also studied and compared. Fónagy et al. demonstrated that 1,4-benzoquinone (1,4-BQ) can be used as a direct e_{CB}⁻ scavenger under anoxic atmosphere, and the amount of the formed 1,4-H₂Q is proportional to that of e_{CB}⁻ generated during the excitation of a photocatalyst [93]. Thus, we used the transformation rate of 1,4-benzoquinone (1,4-BQ) and the formation rate of 1,4-H₂Q to investigate and compare the formation rate of photo-generated e_{CB}⁻. The backward reaction is also possible; reaction between 1,4-H₂Q and h_{VB}⁺ (Equation (2)) results in 1,4-BQ [93,94].



The transformation rate of 1,4-BQ via direct charge transfer in O₂-free suspension highly exceeds that of the COU transformation, mainly based on reactions initiated by •OH in O₂-containing suspension (Table 2). The difference between the efficiency of photocatalysts was observed when LED_{398nm} was applied; the 1,4-BQ transformation was faster for ZnO than TiO₂ (Figure 7d), most probably due to the higher electron mobility of ZnO [89,90]. The transformation was slower for both TiO₂ and ZnO using 398 nm light due to intense reflection at this wavelength and generating fewer e_{CB}[−] – h_{VB}⁺ pairs than 365 nm photons. In both cases, the maximum concentration of 1,4-H₂Q was higher for TiO₂ and just slowly transformed. The 1,4-BQ was present ($c > 2.3 (\pm 0.2) \times 10^{-6}$ M) during the whole treatment time, clearly indicating the backward reaction via h_{VB}⁺ (Equation (2)). In the absence of O₂, the reformed 1,4-BQ (Equation (2)) acts as an e_{CB}[−] acceptor (Equation (1)), which opens up the way for •OH formation (Equation (3)). Most probably, the slow decrease of the sum of 1,4-BQ and 1,4-H₂Q concentrations is caused by •OH initiated transformation ($k_{1,4\text{-BQ} + \bullet\text{OH}} = 1.2 \times 10^9 \text{ M}^{-1} \text{ s}^{-1}$ [95] (Equation (4)); $k_{1,4\text{-H}_2\text{Q} + \bullet\text{OH}} = 5.2 \times 10^9 \text{ M}^{-1} \text{ s}^{-1}$ [96] (Equation (5)) (Figure 7d).

Sulfonamides react fast not only with •OH but also e_{aq}[−]. Mezyk et al. investigated the kinetics and efficiencies of •OH and e_{aq}[−] based reactions to the transformation of four different sulfa drugs (sulfamethazine, sulfamethizole, sulfamethoxazole, and sulfamerazine) [97]. The rate constants of •OH based oxidation ($7.8\text{--}8.5 \times 10^9 \text{ M}^{-1} \text{ s}^{-1}$) and degradation efficiencies were similar (changed from 35% to 53%). The rate constants of reduction with the e_{aq}[−] ($1.0\text{--}2.1 \times 10^{10} \text{ M}^{-1} \text{ s}^{-1}$) was even higher and varied within small ranges, but the corresponding degradation efficiency resulted in highly different values from 0.5% to 71%. They proposed that •OH adds predominantly to the sulfanilic acid ring, while reaction with e_{aq}[−] occurs at different reaction sites of the different heterocyclic rings. The higher transformation rate of SMT and SMP, for ZnO than TiO₂ is probably due to their direct reaction with photogenerated charges. Although the significant contribution of direct charge transfer to the conversion is a possible way to explain the difference of transformation rates observed between TiO₂ and ZnO, it is difficult to interpret the behavior of SMP in the case of TiO₂/LED_{398nm} by this way considering that the number of photogenerated charges is much higher for LED_{365nm}.

3.6. Reaction Mechanism—Effect of Radical Scavenger, Dissolved O₂, and the Quality of TiO₂

Sulfonamides react fast with •OH ($k_{\text{SMT} + \bullet\text{OH}} = 8.3 \times 10^9 \text{ M}^{-1} \text{ s}^{-1}$ [97]); thus, the effect of methanol (MeOH) as •OH-scavenger ($k_{\text{MeOH} + \bullet\text{OH}} = 9.7 \times 10^8 \text{ M}^{-1} \text{ s}^{-1}$ [98]) was investigated. The addition of 2.5×10^{-3} M MeOH to 1.0×10^{-4} M SMT or SMP scavenges more than 70% of •OH reduced the transformation rates to about half in each case (Figure 8) for TiO₂/LED_{398nm}, the SMP transformation was decreased to a similar value than TiO₂/LED_{365nm} or ZnO/LED_{365nm}. MeOH can also be used as a h_{VB}⁺ scavenger [82,99,100]; therefore, it might prevent the direct oxidation of SMP, but this is not a likely explanation in this case. The direct energy transfer is supposed to be the main reason for the photocatalytic isomerization of trans-caffeic acid in TiO₂ suspension [26]. The addition of MeOH completely inhibited the transformation in that case; the effect was much larger than expected based on the radical scavenging capacity of MeOH, similar to its effect on SMP transformation for TiO₂/LED_{398nm}.

Both energy transfer and direct charge transfer could increase the conversion rate, change the reaction pathway, and alter the quality of the primary intermediate. The unique behavior of SMP for TiO₂/LED_{398nm} needed further investigation to clarify since the effect of MeOH was not enough for its proper interpretation, although its high impact indirectly confirmed the role of direct energy transfer.

In O₂ containing suspension, e_{CB}[−] reacts with molecular O₂, which is a source of the ROS formation. The further transformation of O₂^{•−} creates a possibility to the •OH-formation via H₂O₂, while in O₂-free suspension •OH formation is limited to the reaction of H₂O/OH[−] with h_{VB}⁺. In the O₂-free suspension, the initial conversion of SMP is slower but still very significant, especially since most organic compounds are not converted at

all without O_2 . The shape of the kinetic curves is similar in both O_2 -free and aerated suspension: after 45% and 75% removal of SMP, its further transformation became very slow, almost negligible (Figure 9). In both cases, the main intermediate forms via desulfonation, the concentration of hydroxylated products is negligible. The transformation in O_2 -free suspension via direct charge transfer can take place if SMP could behave as e_{CB}^- scavenger instead of O_2 , and both oxidation and reduction of SMP can happen similar to the double electron transfer suggested for the formation of singlet oxygen by Nosaka et al. [21]. Thus, two processes are possible: one is the oxidation and reduction of SMP taking place parallel when different parts of the molecule react with e_{CB}^- and $h\nu_B^+$ or the direct energy transfer, when excited photocatalysts particles transfer energy to SMP, which is finally transformed. If the reaction with ROS or direct charge transfer process is primarily responsible for transforming an organic compound, its conversion is generally negligible in O_2 -free suspension. However, the rapid desulfonation of SMP in an O_2 -free suspension confirms that the energy transfer is primarily responsible for its conversion. Of course, the contribution of the reactions with the formed ROS in the presence of O_2 are not negligible.

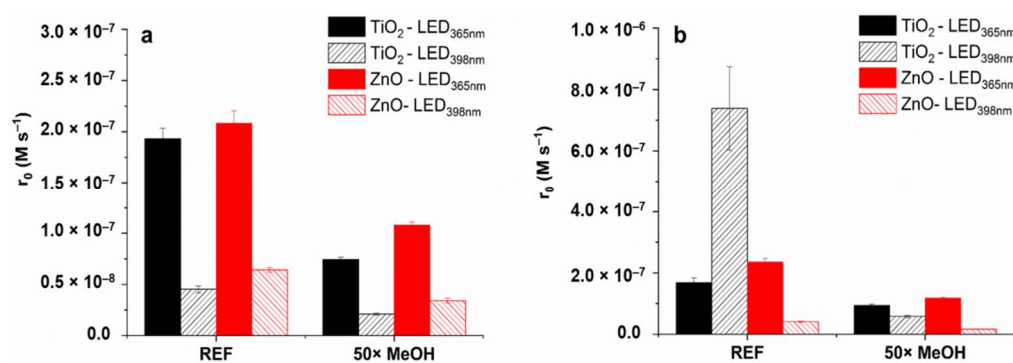


Figure 8. The effect of 2.5×10^{-3} M MeOH on the initial transformation rate of SMT (a) and SMP (b).

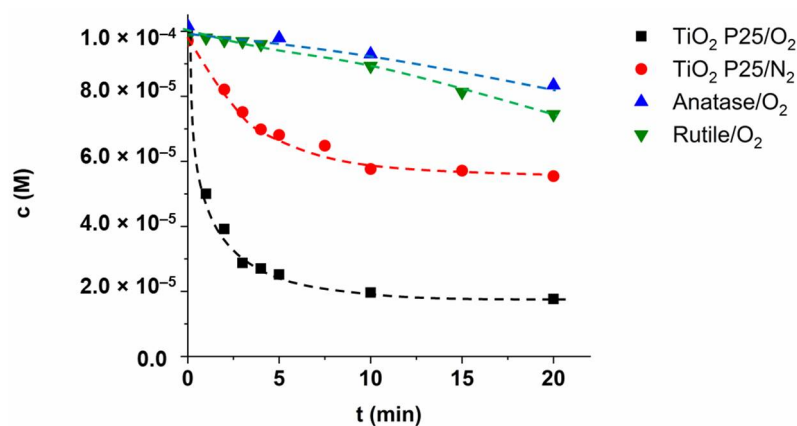


Figure 9. The concentration of SMP in aerated and O_2 -free suspensions using different TiO_2 photocatalysts and LED_{398nm} .

After 5 and 10 min, there is a “breaking point” on the kinetic curves; after that, the SMP transformation is inhibited, especially in O_2 containing suspension. The energy transfer can take place via a different mechanism. In the case of “trivial energy transfer”, SMP absorbs the photon emitted by the excited semiconductor. Unlike the trivial mechanism, Förster and Dexter energy transfers are radiationless processes and strongly depend on the distance of the acceptor from the semiconductor. No electron exchange between acceptor and donor occurs when Förster mechanism takes place, while Dexter energy transfer mechanism occurs when simultaneously two electrons move in opposite directions without net charge exchange. The formed SO_3^{2-}/SO_4^{2-} species and other ions and organic intermediates can adsorb on the TiO_2 surface [101]. The change of catalysts surface can impede the

access to the surface and thus energy transfer via Förster or Dexter mechanism. Moreover, the poisoning of the catalyst surface can also reduce efficiency [102].

The synergistic effect between the two crystal phases resulting in enhanced charge separation and photocatalytic activity was proved by several authors [32,33,103]. Under 398 nm irradiation, mainly the rutile phase excited (Figure 1b), the photogenerated e_{CB}^- can migrate to the anatase phase, inhibiting the recombination of photogenerated charges [104]. Although heterojunction is controversial, the great activity of P25 is undoubted. For determining whether the unique behavior of the SMP is manifested in the case of anatase or rutile phase or characteristic only to the P25, we examined the conversion of SMP in the presence of pure anatase and rutile phase. But only a slow transformation occurred (Figure 9). The intensive desulfonation was not observed. Mainly hydroxylated products formed indicating a $\bullet OH$ based reaction pathway in the case of anatase and rutile.

From this, it can be concluded that the unique transformation of SMP is only possible for TiO₂ P25 and is most likely a consequence of the energy transfer, which takes place in this particular case, using P25 photocatalyst and 398 nm radiation. However, the role of direct charge transfer cannot be excluded, and in O₂-containing suspensions, the $\bullet OH$ -based reaction is likely to contribute to the transformation and mineralization of the products.

3.7. Effect of Matrices on the Removal of Sulfonamides

Experiments were performed with SMT and SMP in two water matrices: tapwater with a low organic and high inorganic content, and biologically treated and filtered domestic wastewater (BTWW) with higher organic and inorganic content (Table S2). For investigation of the inorganic components' effect, transformation rates were determined in suspensions containing the two most abundant anions, Cl⁻ (120 mg dm⁻³) and HCO₃⁻ (525 mg dm⁻³). The concentration of the anions was set to the values measured in the biologically treated wastewater (Table S2).

For SMT, the inhibition effect of matrices was negligible when ZnO photocatalyst was applied, while for TiO₂ decreased by 25 and 50% using LED_{365nm} and LED_{398nm}, respectively (Figure 10a,b). The negative effect of HCO₃⁻ was more pronounced for ZnO (decrease by 34%) than TiO₂, while the effect of Cl⁻ is not significant (Figure 10a). A more enhanced inhibition by the matrices was observed in the case of LED_{398nm}. For SMP, similar observations can be made, except TiO₂/LED_{398nm}, when both matrices and HCO₃⁻ inhibited the SMP transformation completely (Figure 10b,d). Even Cl⁻ is inhibited the conversion, while it had no effect in other cases (Figure 10d).

HCO₃⁻ is a well-known $\bullet OH$ scavenger, but its reaction rate constant is relatively low ($k_{HCO_3^- + \bullet OH} = 1.0 \times 10^{-7} \text{ M}^{-1} \text{ s}^{-1}$ [98]); therefore, it cannot effectively compete for $\bullet OH$ with the sulfonamides. HCO₃⁻ also reported as an efficient scavenger of $h_{\nu B}^+$, resulting in the formation of carbonate radicals (CO₃^{•-}) [61,105] on the surface of TiO₂. The formed CO₃^{•-} is a more selective oxidant than $\bullet OH$, but sulfonamides, especially SMP, are reported to react with it with a high reaction rate constant ($k_{SMT + CO_3^{\bullet-}} = 4.37 \times 10^8 \text{ M}^{-1} \text{ s}^{-1}$, $k_{SMP + CO_3^{\bullet-}} = 8.71 \times 10^8 \text{ M}^{-1} \text{ s}^{-1}$ [106]). The negligible effect of HCO₃⁻ during most of the measurements, and the relatively low effect of the matrices on the transformation rates might be due to the reaction of sulfonamides with formed CO₃^{•-}.

The Cl⁻ does not react with $h_{\nu B}^+$, and generally has a negligible effect on photocatalytic activity using TiO₂ [61]. It may react with $\bullet OH$ with a high reaction rate ($k = 4.3 \times 10^9 \text{ M}^{-1} \text{ s}^{-1}$ [107]) to form chlorine radicals, but at neutral and alkaline pH the backward reaction leading to the reformation of $\bullet OH$ is favored [62]. In the case of ZnO, adsorption of Cl⁻ on the surface can promote the separation of photogenerated charges, leading to higher photocatalytic efficiency [108]. Its significantly negative effect can be observed only for SMP, using TiO₂/LED_{398nm} process. The transformation of SMP using TiO₂ and LED_{398nm} is most likely caused by the energy transfer—with some contribution of the charge transition—which is especially sensitive to the surface conditions.

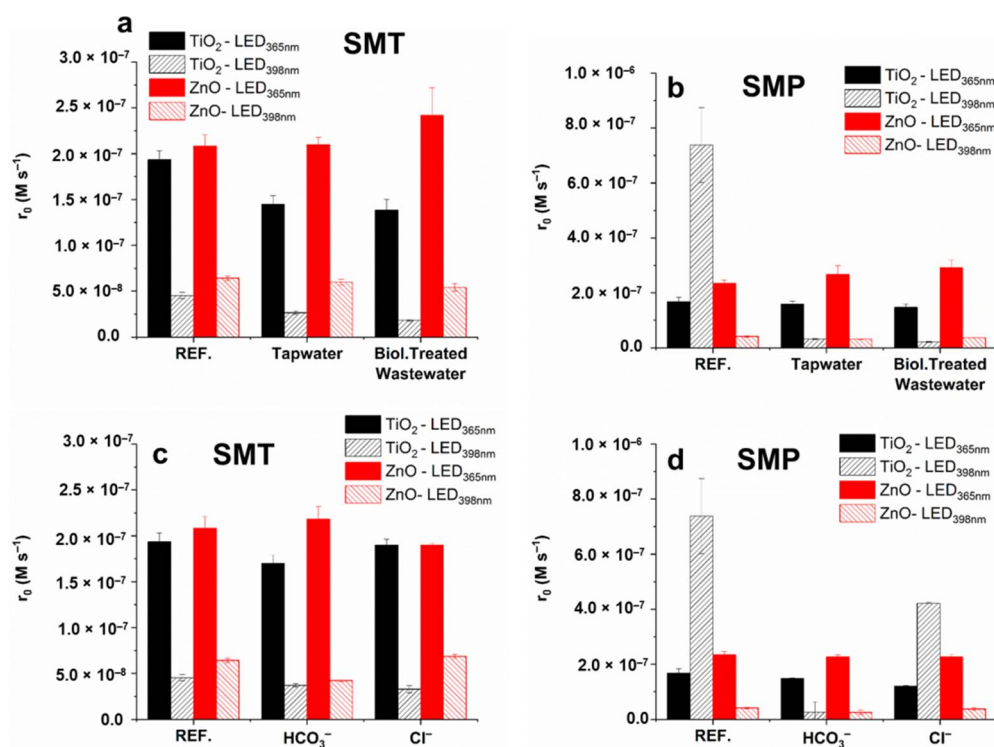


Figure 10. The initial reaction rates of SMT (a,c) and SMP (b,d) determined in purified water (REF), real water matrices (tapwater and biologically treated domestic wastewater), and in the presence of Cl⁻ (120 mg dm⁻³) and HCO₃⁻ (525 mg dm⁻³).

4. Conclusions

Heterogeneous photocatalysis is generally considered to be based primarily on electron transfer reactions at the surface of the irradiated semiconductor. Besides radical-based reactions and direct charge transfer, attention recently moved towards photocatalytic syntheses, requiring selective transformation. Some examples have been reported in the literature when the transformation is due to the energy transfer between excited semiconductor as energy donor, and results in selective transformation of organic substances.

The present work compares the efficiency of the commercially available photocatalysts, TiO₂ and ZnO irradiated with 365 nm or 398 nm. Two sulfonamide antibiotics, SMT and SMP, were used to compare the efficiency of the photocatalysts under 398 and 365 nm radiation. The results showed that, besides •OH-based reaction, the direct charge transfer contributes to the transformation even in the case of ZnO. Consequently, the transformation was faster when ZnO was applied; however, TiO₂ was more efficient in mineralization. The unique behavior, an exceptionally fast transformation of SMP was observed, in the case of TiO₂/LED_{398nm} process, in contrast to the other cases when 365 nm light was more efficient than 398 nm light. The transformation of SMP was fast in both O₂ containing and O₂-free TiO₂ suspensions and takes place via desulfonation, while in other cases, mainly hydroxylated products form. The effect of reaction parameters confirmed that a quite rarely observed direct energy transfer between the excited state P25 and SMP is likely responsible for this unique behavior; however, the role of direct charge transfer cannot be excluded completely.

Our results have highlighted that “non-conventional” mechanisms can occur in exceptional cases during heterogeneous photocatalysis (even in the case of the well-known photocatalyst, such as TiO₂), and the effect of wavelength is also worth investigating. The presented results may contribute to further studies on the application of photocatalysts, either in the selective removal of organic pollutants or in the field of organic chemical synthesis.

Supplementary Materials: The following supporting information can be downloaded at: <https://www.mdpi.com/article/10.3390/ma15010049/s1>, Figure S1: The schematic figure of the photoreactors (a: LED_{365nm}, b: LED_{398nm}); Figure S2: The peak area (HPLC-DAD) of the products of SMT transformation as a function of irradiation time; Figure S3: The peak area (HPLC-DAD) of the products of SMP transformation as a function of irradiation time; Figure S4: The transformation of organic nitrogen and sulfur to inorganic ions during the photocatalytic removal of SMT (Mineralization(%) = concentration of given ion divided by the organic N-content or S-content of the starting solution); Figure S5: The transformation of organic nitrogen and sulfur to inorganic ions during the photocatalytic removal of SMP (Mineralization(%) = concentration of given ion divided by the organic N-content or S-content of the starting solution); Table S1: The list of used chemicals, their distributors and purity; Table S2: The measured, relevant parameters of the real water matrices.

Author Contributions: M.N.: experimental work, visualization, writing and editing the initial draft; L.F.: experimental work and editing; G.B.: ionchromatography measurement; G.K.: XRD and DRS measurement; K.H.: review and evaluation; T.A.: conceptualization; formulating and managing research goals and work, evaluating results, writing—review & editing. All authors have read and agreed to the published version of the manuscript.

Funding: Tünde Alapi acknowledges the support of the János Bolyai Research Scholarship of the Hungarian Academy of Sciences. The work was financed by the New National Excellence Program of the Ministry for Innovation and Technology (ÚNKP-21-4-SZTE-494, and ÚNKP-21-5-SZTE-594) and the National Research, Development and Innovation Office-NKFI Fund OTKA, project number FK132742.

Data Availability Statement: The data is included in the article or Supplementary Material.

Conflicts of Interest: The authors declare no conflict of interest.

References

1. Tacconelli, E.; Carrara, E.; Savoldi, A.; Harbarth, S.; Mendelson, M.; Monnet, D.L.; Pulcini, C.; Kahlmeter, G.; Kluytmans, J.; Carmeli, Y.; et al. Discovery, Research, and Development of New Antibiotics: The WHO Priority List of Antibiotic-Resistant Bacteria and Tuberculosis. *Lancet Infect. Dis.* **2018**, *18*, 318–327. [[CrossRef](#)]
2. Falowo, A.B.; Akimoladun, O.F. Veterinary drug residues in meat and meat products: Occurrence, detection and implications. In *Veterinary Medicine and Pharmaceuticals*; Bekoe, S.O., Saravanan, M., Eds.; IntechOpen: London, UK, 2020. [[CrossRef](#)]
3. Tacic, A.; Nikolic, V.; Nikolic, L.; Savic, I. Antimicrobial Sulfonamide Drugs. *Adv. Technol.* **2017**, *6*, 58–71. [[CrossRef](#)]
4. Klauson, D.; Romero Sarcos, N.; Krichevskaya, M.; Kattel, E.; Dulova, N.; Dedova, T.; Trapido, M. Advanced Oxidation Processes for Sulfonamide Antibiotic Sulfamethizole Degradation: Process Applicability Study at ppm Level and Scale-down to ppb Level. *J. Environ. Chem. Eng.* **2019**, *7*, 103287. [[CrossRef](#)]
5. Wang, J.; Chu, L.; Wojnárovits, L.; Takács, E. Occurrence and Fate of Antibiotics, Antibiotic Resistant Genes (ARGs) and Antibiotic Resistant Bacteria (ARB) in Municipal Wastewater Treatment Plant: An Overview. *Sci. Total Environ.* **2020**, *744*, 140997. [[CrossRef](#)]
6. Mendiola-Alvarez, S.Y.; Palomino-Cabello, C.; Hernández-Ramírez, A.; Turnes-Palomino, G.; Guzmán-Mar, J.L.; Hinojosa-Reyes, L. Coupled Heterogeneous Photocatalysis Using a P-TiO₂-AFe₂O₃ Catalyst and K₂S₂O₈ for the Efficient Degradation of a Sulfonamide Mixture. *J. Photochem. Photobiol. A Chem.* **2020**, *394*, 112485. [[CrossRef](#)]
7. Li, P.; Guo, M.; Wang, Q.; Li, Z.; Wang, C.C.C.; Chen, N.; Wang, C.C.C.; Wan, C.; Chen, S. Controllable Synthesis of Cerium Zirconium Oxide Nanocomposites and Their Application for Photocatalytic Degradation of Sulfonamides. *Appl. Catal. B Environ.* **2019**, *259*, 118107. [[CrossRef](#)]
8. Estrada-Flórez, S.E.; Serna-Galvis, E.A.; Torres-Palma, R.A. Photocatalytic vs. Sonochemical Removal of Antibiotics in Water: Structure-Degradability Relationship, Mineralization, Antimicrobial Activity, and Matrix Effects. *J. Environ. Chem. Eng.* **2020**, *8*, 104359. [[CrossRef](#)]
9. Wu, C.H.; Kuo, C.Y.; Dong, C.D.; Chen, C.W.; Lin, Y.L. Removal of Sulfonamides from Wastewater in the UV/TiO₂ System: Effects of PH and Salinity on Photodegradation and Mineralization. *Water Sci. Technol.* **2019**, *79*, 349–355. [[CrossRef](#)] [[PubMed](#)]
10. Zhang, J.; Li, J.; Su, H.; Zhao, Y.; Zeng, X.; Hu, M.; Xiao, W.; Mao, X. H-Bonding Effect of Oxyanions Enhanced Photocatalytic Degradation of Sulfonamides by g-C₃N₄ in Aqueous Solution. *J. Hazard. Mater.* **2019**, *366*, 259–267. [[CrossRef](#)]
11. Song, Y.; Tian, J.; Gao, S.; Shao, P.; Qi, J.; Cui, F. Photodegradation of Sulfonamides by G-C₃N₄ under Visible Light Irradiation: Effectiveness, Mechanism and Pathways. *Appl. Catal. B Environ.* **2017**, *210*, 88–96. [[CrossRef](#)]
12. Chen, P.; Zhang, Q.; Zheng, X.; Tan, C.; Zhuo, M.; Chen, T.; Wang, F.; Liu, H.; Liu, Y.; Feng, Y.; et al. Phosphate-Modified m-Bi₂O₄ Enhances the Absorption and Photocatalytic Activities of Sulfonamide: Mechanism, Reactive Species, and Reactive Sites. *J. Hazard. Mater.* **2020**, *384*, 121443. [[CrossRef](#)]
13. Wang, W.; Tian, J.; Zhu, Z.; Zhu, C.; Liu, B.; Hu, C. Insight into Quinolones and Sulfonamides Degradation, Intermediate Product Identification and Decomposition Pathways with the Assistance of Bi₂MoO₆/Bi₂WO₆/MWCNTs Photocatalyst. *Process Saf. Environ. Prot.* **2021**, *147*, 527–546. [[CrossRef](#)]

14. Zhu, W.; Sun, F.; Goei, R.; Zhou, Y. Facile Fabrication of RGO-WO₃ Composites for Effective Visible Light Photocatalytic Degradation of Sulfamethoxazole. *Appl. Catal. B Environ.* **2017**, *207*, 93–102. [[CrossRef](#)]
15. Yang, C.C.; Huang, C.L.; Cheng, T.C.; Lai, H.T. Inhibitory Effect of Salinity on the Photocatalytic Degradation of Three Sulfonamide Antibiotics. *Int. Biodeterior. Biodegrad.* **2015**, *102*, 116–125. [[CrossRef](#)]
16. Kaniou, S.; Pitarakis, K.; Barlagianni, I.; Poulios, I. Photocatalytic Oxidation of Sulfamethazine. *Chemosphere* **2005**, *60*, 372–380. [[CrossRef](#)] [[PubMed](#)]
17. Baran, W.; Sochacka, J.; Wardas, W. Toxicity and Biodegradability of Sulfonamides and Products of Their Photocatalytic Degradation in Aqueous Solutions. *Chemosphere* **2006**, *65*, 1295–1299. [[CrossRef](#)]
18. Ahmed, S.; Rasul, M.G.; Brown, R.; Hashib, M.A. Influence of Parameters on the Heterogeneous Photocatalytic Degradation of Pesticides and Phenolic Contaminants in Wastewater: A Short Review. *J. Environ. Manag.* **2011**, *92*, 311–330. [[CrossRef](#)] [[PubMed](#)]
19. Younis, S.A.; Kim, K.H. Heterogeneous Photocatalysis Scalability for Environmental Remediation: Opportunities and Challenges. *Catalysts* **2020**, *11*, 1109. [[CrossRef](#)]
20. Bellardita, M.; Ceccato, R.; Dirè, S.; Loddo, V.; Palmisano, L.; Parrino, F. Energy Transfer in Heterogeneous Photocatalysis. *Subst. Int. J. Hist. Chem.* **2019**, *3*, 49–57. [[CrossRef](#)]
21. Nosaka, Y.; Daimon, T.; Nosaka, A.Y.; Murakami, Y. Singlet Oxygen Formation in Photocatalytic TiO₂ Aqueous Suspension. *Phys. Chem. Chem. Phys.* **2004**, *6*, 2917–2918. [[CrossRef](#)]
22. Jańczyk, A.; Krakowska, E.; Stochel, G.; Macyk, W. Singlet Oxygen Photogeneration at Surface Modified Titanium Dioxide. *J. Am. Chem. Soc.* **2006**, *128*, 15574–15575. [[CrossRef](#)] [[PubMed](#)]
23. Buchalska, M.; Łabuz, P.; Bujak, Ł.; Szewczyk, G.; Sarna, T.; Maćkowski, S.; Macyk, W. New Insight into Singlet Oxygen Generation at Surface Modified Nanocrystalline TiO₂— the Effect of near-Infrared Irradiation. *J. Chem. Soc. Dalt. Trans.* **2013**, *42*, 9468–9475. [[CrossRef](#)]
24. Ciriminna, R.; Parrino, F.; De Pasquale, C.; Palmisano, L.; Pagliaro, M. Photocatalytic Partial Oxidation of Limonene to 1,2 Limonene Oxide. *Chem. Commun.* **2018**, *54*, 1008–1011. [[CrossRef](#)]
25. Parrino, F.; Fidalgo, A.; Palmisano, L.; Ilharco, L.M.; Pagliaro, M.; Ciriminna, R. Polymers of Limonene Oxide and Carbon Dioxide: Polycarbonates of the Solar Economy. *ACS Omega* **2018**, *3*, 4884–4890. [[CrossRef](#)] [[PubMed](#)]
26. Parrino, F.; Di Paola, A.; Loddo, V.; Pibiri, I.; Bellardita, M.; Palmisano, L. Photochemical and Photocatalytic Isomerization of Trans-Caffeic Acid and Cyclization of Cis-Caffeic Acid to Esculetin. *Appl. Catal. B Environ.* **2016**, *182*, 347–355. [[CrossRef](#)]
27. Srikant, V.; Clarke, D.R. On the Optical Band Gap of Zinc Oxide. *J. Appl. Phys.* **1998**, *83*, 5447–5451. [[CrossRef](#)]
28. Kafizas, A.; Wang, X.; Pendlebury, S.R.; Barnes, P.; Ling, M.; Sotelo-Vazquez, C.; Quesada-Cabrera, R.; Li, C.; Parkin, I.P.; Durrant, J.R. Where Do Photogenerated Holes Go in Anatase:Rutile TiO₂? A Transient Absorption Spectroscopy Study of Charge Transfer and Lifetime. *J. Phys. Chem. A* **2016**, *120*, 715–723. [[CrossRef](#)]
29. Rohilla, S.; Gupta, A.; Kumar, V.; Kumari, S.; Petru, M.; Amor, N.; Noman, M.T.; Dalal, J. Excellent Uv-light Triggered Photocatalytic Performance of ZnO:SiO₂ Nanocomposite for Water Pollutant Compound Methyl Orange Dye. *Nanomaterials* **2021**, *11*, 2548. [[CrossRef](#)] [[PubMed](#)]
30. Ohno, T.; Sarukawa, K.; Tokieda, K.; Matsumura, M. Morphology of a TiO₂ Photocatalyst (Degussa, P-25) Consisting of Anatase and Rutile Crystalline Phases. *J. Catal.* **2001**, *203*, 82–86. [[CrossRef](#)]
31. Datye, A.K.; Riegel, G.; Bolton, J.R.; Huang, M.; Prairie, M.R. Microstructural Characterization of a Fumed Titanium Dioxide Photocatalyst. *J. Solid State Chem.* **1995**, *115*, 236–239. [[CrossRef](#)]
32. Bickley, R.I.; Gonzalez-Carreno, T.; Lees, J.S.; Palmisano, L.; Tilley, R.J.D. A Structural Investigation of Titanium Dioxide Photocatalysts. *J. Solid State Chem.* **1991**, *92*, 178–190. [[CrossRef](#)]
33. Hurum, D.C.; Agrios, A.G.; Gray, K.A.; Rajh, T.; Thurnauer, M.C. Explaining the Enhanced Photocatalytic Activity of Degussa P25 Mixed-Phase TiO₂ Using EPR. *J. Phys. Chem. B* **2003**, *107*, 4545–4549. [[CrossRef](#)]
34. MacDonald, I.R.; Howe, R.F.; Zhang, X.; Zhou, W. In Situ EPR Studies of Electron Trapping in a Nanocrystalline Rutile. *J. Photochem. Photobiol. A Chem.* **2010**, *216*, 238–243. [[CrossRef](#)]
35. MacDonald, I.R.; Rhydderch, S.; Holt, E.; Grant, N.; Storey, J.M.D.; Howe, R.F. EPR Studies of Electron and Hole Trapping in Titania Photocatalysts. *Catal. Today* **2012**, *182*, 39–45. [[CrossRef](#)]
36. Jiang, X.; Manawan, M.; Feng, T.; Qian, R.; Zhao, T.; Zhou, G.; Kong, F.; Wang, Q.; Dai, S.; Pan, J.H. Anatase and Rutile in Evonik Aeroxide P25: Heterojunctioned or Individual Nanoparticles? *Catal. Today* **2018**, *300*, 12–17. [[CrossRef](#)]
37. Ohtani, B.; Prieto-Mahaney, O.O.; Li, D.; Abe, R. What Is Degussa (Evonic) P25? Crystalline Composition Analysis, Reconstruction from Isolated Pure Particles and Photocatalytic Activity Test. *J. Photochem. Photobiol. A Chem.* **2010**, *216*, 179–182. [[CrossRef](#)]
38. Prieto-Mahaney, O.O.; Murakami, N.; Abe, R.; Ohtani, B. Correlation between Photoeatalytic Activities and Structural and Physical Properties of Titanium(IV) Oxide Powders. *Chem. Lett.* **2009**, *38*, 238–239. [[CrossRef](#)]
39. Ide, Y.; Inami, N.; Hattori, H.; Saito, K.; Sohmiya, M.; Tsumoji, N.; Komaguchi, K.; Sano, T.; Bando, Y.; Golberg, D.; et al. Remarkable Charge Separation and Photocatalytic Efficiency Enhancement through Interconnection of TiO₂ Nanoparticles by Hydrothermal Treatment. *Angew. Chem. Int. Ed.* **2016**, *55*, 3600–3605. [[CrossRef](#)]
40. Zhang, H.; Chen, G.; Bahnemann, D.W. Photoelectrocatalytic Materials for Environmental Applications. *J. Mater. Chem.* **2009**, *19*, 5089–5121. [[CrossRef](#)]
41. Deng, X.; Chen, Y.; Wen, J.; Xu, Y.; Zhu, J.; Bian, Z. Polyaniline-TiO₂ Composite Photocatalysts for Light-Driven Hexavalent Chromium Ions Reduction. *Sci. Bull.* **2020**, *65*, 105–112. [[CrossRef](#)]

42. Tang, B.; Chen, H.; Peng, H.; Wang, Z.; Huang, W. Graphene Modified TiO₂ Composite Photocatalysts: Mechanism, Progress and Perspective. *Nanomaterials* **2018**, *8*, 105. [[CrossRef](#)]
43. Qin, R.; Meng, F.; Khan, M.W.; Yu, B.; Li, H.; Fan, Z.; Gong, J. Fabrication and Enhanced Photocatalytic Property of TiO₂-ZnO Composite Photocatalysts. *Mater. Lett.* **2019**, *240*, 84–87. [[CrossRef](#)]
44. Kumari, S.; Malik, S.; Kumar, S.; Dalal, J.; Dahiya, S.; Ohlan, A.; Punia, R.; Maan, A.S. Excellent Photoelectrical Properties of ZnO Thin Film Based on ZnO /Epoxy-Resin Ink for UV-Light Detectors. *AIP Conf. Proc.* **2019**, *2142*, 120004. [[CrossRef](#)]
45. Dossin Zanrosso, C.; Piazza, D.; Lansarin, M.A. PVDF/ZnO Composite Films for Photocatalysis: A Comparative Study of Solution Mixing and Melt Blending Methods. *Polym. Eng. Sci.* **2020**, *60*, 1146–1157. [[CrossRef](#)]
46. Mirikaram, N.; Pérez-molina, Á.; Morales-torres, S.; Salemi, A.; Maldonado-hódar, F.J.; Pastrana-martínez, L.M. Photocatalytic Performance of ZnO-graphene Oxide Composites towards the Degradation of Vanillic Acid under Solar Radiation and Visibleled. *Nanomaterials* **2021**, *11*, 1576. [[CrossRef](#)]
47. Raha, S.; Mohanta, D.; Ahmaruzzaman, M. Novel CuO/Mn₃O₄/ZnO Nanocomposite with Superior Photocatalytic Activity for Removal of Rabeprazole from Water. *Sci. Rep.* **2021**, *11*, 15187. [[CrossRef](#)] [[PubMed](#)]
48. Thangadurai, P.; Beura, R.; Kumar, J.S. Nanomaterials with different morphologies for photocatalysis. In *Green Photocatalysts*; Naushad, M., Rajendran, S., Lichfouse, E., Eds.; Springer: Berlin/Heidelberg, Germany, 2020; ISBN 9783540228608.
49. Yang, H.; Li, G.; An, T.; Gao, Y.; Fu, J. Photocatalytic Degradation Kinetics and Mechanism of Environmental Pharmaceuticals in Aqueous Suspension of TiO₂: A Case of Sulfa Drugs. *Catal. Today* **2010**, *153*, 200–207. [[CrossRef](#)]
50. Mirzaei, A.; Yerushalmi, L.; Chen, Z.; Haghghat, F.; Guo, J. Enhanced Photocatalytic Degradation of Sulfamethoxazole by Zinc Oxide Photocatalyst in the Presence of Fluoride Ions: Optimization of Parameters and Toxicological Evaluation. *Water Res.* **2018**, *132*, 241–251. [[CrossRef](#)] [[PubMed](#)]
51. Náfrádi, M.; Hernadi, K.; Kónya, Z.; Alapi, T. Investigation of the Efficiency of BiOI/BiOCl Composite Photocatalysts Using UV, Cool and Warm White LED Light Sources-Photon Efficiency, Toxicity, Reusability, Matrix Effect, and Energy Consumption. *Chemosphere* **2021**, *280*, 130636. [[CrossRef](#)] [[PubMed](#)]
52. Khan, J.A.; Sayed, M.; Khan, S.; Shah, N.S.; Dionysiou, D.D.; Boczkaj, G. Advanced oxidation processes for the treatment of contaminants of emerging concern. In *Contaminants of Emerging Concern in Water and Wastewater*; Hernandez-Maldonado, A., Blaney, L., Eds.; Elsevier Inc.: Amsterdam, The Netherlands, 2019; ISBN 9780128135617.
53. Bertagna Silva, D.; Buttiglieri, G.; Babić, S. State-of-the-Art and Current Challenges for TiO₂/UV-LED Photocatalytic Degradation of Emerging Organic Micropollutants. *Environ. Sci. Pollut. Res.* **2021**, *28*, 103–120. [[CrossRef](#)] [[PubMed](#)]
54. Jo, W.K.; Tayade, R.J. New Generation Energy-Efficient Light Source for Photocatalysis: LEDs for Environmental Applications. *Ind. Eng. Chem. Res.* **2014**, *53*, 2073–2084. [[CrossRef](#)]
55. Tokode, O.; Prabhu, R.; Lawton, L.A.; Robertson, P.K.J. UV LED Sources for Heterogeneous Photocatalysis. *Handb. Environ. Chem.* **2015**, *35*, 159–179. [[CrossRef](#)]
56. Eskandarian, M.R.; Choi, H.; Fazli, M.; Rasoulifard, M.H. Effect of UV-LED Wavelengths on Direct Photolytic and TiO₂ Photocatalytic Degradation of Emerging Contaminants in Water. *Chem. Eng. J.* **2016**, *300*, 414–422. [[CrossRef](#)]
57. Biancullo, F.; Moreira, N.F.F.; Ribeiro, A.R.; Manaia, C.M.; Faria, J.L.; Nunes, O.C.; Castro-Silva, S.M.; Silva, A.M.T. Heterogeneous Photocatalysis Using UVA-LEDs for the Removal of Antibiotics and Antibiotic Resistant Bacteria from Urban Wastewater Treatment Plant Effluents. *Chem. Eng. J.* **2019**, *367*, 304–313. [[CrossRef](#)]
58. Takeda, K.; Fujisawa, K.; Nojima, H.; Kato, R.; Ueki, R.; Sakugawa, H. Hydroxyl Radical Generation with a High Power Ultraviolet Light Emitting Diode (UV-LED) and Application for Determination of Hydroxyl Radical Reaction Rate Constants. *J. Photochem. Photobiol. A Chem.* **2017**, *340*, 8–14. [[CrossRef](#)]
59. Taghavi, M.; Ghaneian, M.T.; Ehrampoush, M.H.; Tabatabaee, M.; Afsharnia, M.; Alami, A.; Mardaneh, J. Feasibility of Applying the LED-UV-Induced TiO₂/ZnO-Supported H₃PMo₁₂O₄₀ Nanoparticles in Photocatalytic Degradation of Aniline. *Environ. Monit. Assess.* **2018**, *190*, 188. [[CrossRef](#)] [[PubMed](#)]
60. Khademalrasool, M.; Farbod, M.; Talebzadeh, M.D. The Improvement of Photocatalytic Processes: Design of a Photoreactor Using High-Power LEDs. *J. Sci. Adv. Mater. Devices* **2016**, *1*, 382–387. [[CrossRef](#)]
61. Farner Budarz, J.; Turolla, A.; Piasecki, A.F.; Bottero, J.Y.; Antonelli, M.; Wiesner, M.R. Influence of Aqueous Inorganic Anions on the Reactivity of Nanoparticles in TiO₂ Photocatalysis. *Langmuir* **2017**, *33*, 2770–2779. [[CrossRef](#)] [[PubMed](#)]
62. Bouanimba, N.; Laid, N.; Zouaghi, R.; Sehili, T. A Comparative Study of the Activity of TiO₂ Degussa P25 and Millennium PCs in the Photocatalytic Degradation of Bromothymol Blue. *Int. J. Chem. React. Eng.* **2018**, *16*, 1–19. [[CrossRef](#)]
63. Serrà, A.; Philippe, L.; Perreault, F.; Garcia-Segura, S. Photocatalytic Treatment of Natural Waters. Reality or Hype? The Case of Cyanotoxins Remediation. *Water Res.* **2021**, *188*, 116543. [[CrossRef](#)]
64. Tufail, A.; Price, W.E.; Mohseni, M.; Pramanik, B.K.; Hai, F.I. A Critical Review of Advanced Oxidation Processes for Emerging Trace Organic Contaminant Degradation: Mechanisms, Factors, Degradation Products, and Effluent Toxicity. *J. Water Process Eng.* **2021**, *40*, 101778. [[CrossRef](#)]
65. Kudlek, E.; Dudziak, M.; Bohdziewicz, J. Influence of Inorganic Ions and Organic Substances on the Degradation of Pharmaceutical Compound in Water Matrix. *Water* **2016**, *8*, 532. [[CrossRef](#)]
66. Guillard, C.; Puzenat, E.; Lachheb, H.; Houas, A.; Herrmann, J.M. Why Inorganic Salts Decrease the TiO₂ Photocatalytic Efficiency. *Int. J. Photoenergy* **2005**, *7*, 641208. [[CrossRef](#)]

67. Šojić Merkulov, D.V.; Lazarević, M.J.; Despotović, V.N.; Banić, N.D.; Finčur, N.L.; Maletić, S.P.; Abramović, B.F. The Effects of Inorganic Anions and Organic Matter on Mesotrione (Callisto[®]) Removal from Environmental Waters. *J. Serbian Chem. Soc.* **2017**, *82*, 343–355. [[CrossRef](#)]
68. Lado Ribeiro, A.R.; Moreira, N.F.F.; Li Puma, G.; Silva, A.M.T. Impact of Water Matrix on the Removal of Micropollutants by Advanced Oxidation Technologies. *Chem. Eng. J.* **2019**, *363*, 155–173. [[CrossRef](#)]
69. Hatchard, C.G.; Parker, C.A. A New Sensitive Chemical Actinometer-II. Potassium Ferrioxalate as a Standard Chemical Actinometer. *Proc. R. Soc. London Ser. A Math. Phys. Sci.* **1956**, *235*, 518–536. [[CrossRef](#)]
70. Zuccheri, T.; Colonna, M.; Stefanini, I.; Santini, C.; Di Gioia, D. Bactericidal Activity of Aqueous Acrylic Paint Dispersion for Wooden Substrates Based on TiO₂ Nanoparticles Activated by Fluorescent Light. *Materials* **2013**, *6*, 3270–3283. [[CrossRef](#)]
71. Hassellöv, M.; Readman, J.W.; Ranville, J.F.; Tiede, K. Nanoparticle Analysis and Characterization Methodologies in Environmental Risk Assessment of Engineered Nanoparticles. *Ecotoxicology* **2008**, *17*, 344–361. [[CrossRef](#)]
72. White, L.; Koo, Y.; Yun, Y.; Sankar, J. TiO₂ Deposition on AZ31 Magnesium Alloy Using Plasma Electrolytic Oxidation. *J. Nanomater.* **2013**, *2013*, 11. [[CrossRef](#)]
73. Thamaphat, K.; Limsuwan, P.; Ngotawornchai, B. Phase Characterization of TiO₂ Powder by XRD and TEM. *Agric. Nat. Resour.* **2008**, *42*, 357–361.
74. Arefi, M.R.; Rezaei-Zarchi, S. Synthesis of Zinc Oxide Nanoparticles and Their Effect on the Compressive Strength and Setting Time of Self-Compacted Concrete Paste as Cementitious Composites. *Int. J. Mol. Sci.* **2012**, *13*, 4340–4350. [[CrossRef](#)]
75. Yi, Z.; Wang, J.; Jiang, T.; Tang, Q.; Cheng, Y. Photocatalytic Degradation of Sulfamethazine in Aqueous Solution Using ZnO with Different Morphologies. *R. Soc. Open Sci.* **2018**, *5*, 171457. [[CrossRef](#)]
76. Zhu, G.; Sun, Q.; Wang, C.; Yang, Z.; Xue, Q. Removal of Sulfamethoxazole, Sulfathiazole and Sulfamethazine in Their Mixed Solution by UV/H₂O₂ Process. *Int. J. Environ. Res. Public Health* **2019**, *16*, 1797. [[CrossRef](#)] [[PubMed](#)]
77. Shah, S.; Hao, C. Quantum Chemical Investigation on Photodegradation Mechanisms of Sulfamethoxy pyridazine with Dissolved Inorganic Matter and Hydroxyl Radical. *J. Environ. Sci.* **2017**, *57*, 85–92. [[CrossRef](#)]
78. Guo, C.; Xu, J.; Wang, S.; Zhang, Y.; He, Y.; Li, X. Photodegradation of Sulfamethazine in an Aqueous Solution by a Bismuth Molybdate Photocatalyst. *Catal. Sci. Technol.* **2013**, *3*, 1603–1611. [[CrossRef](#)]
79. Yang, L.; Shi, Y.; Li, J.; Fang, L.; Luan, T. Transformation of Aqueous Sulfonamides under Horseradish Peroxidase and Characterization of Sulfur Dioxide Extrusion Products from Sulfadiazine. *Chemosphere* **2018**, *200*, 164–172. [[CrossRef](#)]
80. Boreen, A.L.; Arnold, W.A.; McNeill, K. Triplet-Sensitized Photodegradation of Sulfa Drugs Containing Six-Membered Heterocyclic Groups: Identification of an SO₂ Extrusion Photoproduct. *Environ. Sci. Technol.* **2005**, *39*, 3630–3638. [[CrossRef](#)]
81. Ge, L.; Zhang, P.; Halsall, C.; Li, Y.; Chen, C.E.; Li, J.; Sun, H.; Yao, Z. The Importance of Reactive Oxygen Species on the Aqueous Phototransformation of Sulfonamide Antibiotics: Kinetics, Pathways, and Comparisons with Direct Photolysis. *Water Res.* **2019**, *149*, 243–250. [[CrossRef](#)]
82. Park, S.; Kim, H.J.; Kim, J.S.; Yoo, K.; Lee, J.C.; Anderson, W.A.; Lee, J.H. Photocatalytic Reduction of Nitrate in Wastewater Using ZnO Nanopowder Synthesized by Solution Combustion Method. *J. Nanosci. Nanotechnol.* **2007**, *7*, 4069–4072. [[CrossRef](#)] [[PubMed](#)]
83. Løgager, T.; Sehested, K. Formation and Decay of Peroxynitric Acid: A Pulse Radiolysis Study. *J. Phys. Chem.* **1993**, *97*, 10047–10052. [[CrossRef](#)]
84. Náfrádi, M.; Farkas, L.; Alapi, T.; Hernádi, K.; Kovács, K.; Wojnárovits, L.; Takács, E. Application of Coumarin and Coumarin-3-Carboxylic Acid for the Determination of Hydroxyl Radicals during Different Advanced Oxidation Processes. *Radiat. Phys. Chem.* **2020**, *170*, 108610. [[CrossRef](#)]
85. Ishibashi, K.I.; Fujishima, A.; Watanabe, T.; Hashimoto, K. Detection of Active Oxidative Species in TiO₂ Photocatalysis Using the Fluorescence Technique. *Electrochem. Commun.* **2000**, *2*, 207–210. [[CrossRef](#)]
86. Zhang, J.; Nosaka, Y. Quantitative Detection of OH Radicals for Investigating the Reaction Mechanism of Various Visible-Light TiO₂ Photocatalysts in Aqueous Suspension. *J. Phys. Chem. C* **2013**, *117*, 1383–1391. [[CrossRef](#)]
87. Zhang, J.; Nosaka, Y. Generation of OH Radicals and Oxidation Mechanism in Photocatalysis of WO₃ and BiVO₄ Powders. *J. Photochem. Photobiol. A Chem.* **2015**, *303–304*, 53–58. [[CrossRef](#)]
88. Černigoj, U.; Štangar, U.L.; Trebše, P.; Sarakha, M. Determination of Catalytic Properties of TiO₂ Coatings Using Aqueous Solution of Coumarin: Standardization Efforts. *J. Photochem. Photobiol. A Chem.* **2009**, *201*, 142–150. [[CrossRef](#)]
89. Baxter, J.B.; Schmuttenmaer, C.A. Conductivity of ZnO Nanowires, Nanoparticles, and Thin Films Using Time-Resolved Terahertz Spectroscopy. *J. Phys. Chem. B* **2006**, *110*, 25229–25239. [[CrossRef](#)] [[PubMed](#)]
90. Meulenkamp, E.A. Electron Transport in Nanoparticulate ZnO Films. *J. Phys. Chem. B* **1999**, *103*, 7831–7838. [[CrossRef](#)]
91. Sachs, M.; Pastor, E.; Kafizas, A.; Durrant, J.R. Evaluation of Surface State Mediated Charge Recombination in Anatase and Rutile TiO₂. *J. Phys. Chem. Lett.* **2016**, *7*, 3742–3746. [[CrossRef](#)]
92. Tang, J.; Durrant, J.R.; Klug, D.R. Mechanism of Photocatalytic Water Splitting in TiO₂. Reaction of Water with Photoholes, Importance of Charge Carrier Dynamics, and Evidence for Four-Hole Chemistry. *J. Am. Chem. Soc.* **2008**, *130*, 13885–13891. [[CrossRef](#)] [[PubMed](#)]
93. Fónagy, O.; Szabó-Bárdos, E.; Horváth, O. 1,4-Benzoquinone and 1,4-Hydroquinone Based Determination of Electron and Superoxide Radical Formed in Heterogeneous Photocatalytic Systems. *J. Photochem. Photobiol. A Chem.* **2021**, *407*, 113057. [[CrossRef](#)]

94. Henderson, M.A.; Shen, M. Electron-Scavenging Chemistry of Benzoquinone on TiO₂(110). *Top. Catal.* **2017**, *60*, 440–445. [[CrossRef](#)]
95. Adams, G.E.; Michael, B.D. Pulse Radiolysis of Benzoquinone and Hydroquinone. Semiquinone Formation by Water Elimination from Trihydroxycyclohexadienyl Radicals. *Trans. Faraday Soc.* **1967**, *63*, 1171–1180. [[CrossRef](#)]
96. Al-Suhybani, A.A.; Hughes, G. Pulse Radiolysis of Hydroquinone Solutions in the Presence of N₂O and O₂. *Isot. Environ. Heal. Stud.* **1985**, *21*, 208–210. [[CrossRef](#)]
97. Mezyk, S.P.; Neubauer, T.J.; Cooper, W.J.; Peller, J.R. Free-Radical-Induced Oxidative and Reductive Degradation of Sulfa Drugs in Water: Absolute Kinetics and Efficiencies of Hydroxyl Radical and Hydrated Electron Reactions. *J. Phys. Chem. A* **2007**, *111*, 9019–9024. [[CrossRef](#)]
98. Buxton, G.V.; Greenstock, C.L.; Helman, W.P.; Ross, A.B. Critical Review of Rate Constants for Reactions of Hydrated Electrons, Hydrogen Atoms and Hydroxyl Radicals (OH/O⁻ in Aqueous Solution. *J. Phys. Chem. Ref. Data* **1988**, *17*, 513–886. [[CrossRef](#)]
99. Nguyen, V.N.H.; Amal, R.; Beydoun, D. Effect of Formate and Methanol on Photoreduction/Removal of Toxic Cadmium Ions Using TiO₂ Semiconductor as Photocatalyst. *Chem. Eng. Sci.* **2003**, *58*, 4429–4439. [[CrossRef](#)]
100. Zhang, J.; Nosaka, Y. Photocatalytic Oxidation Mechanism of Methanol and the Other Reactants in Irradiated TiO₂ Aqueous Suspension Investigated by OH Radical Detection. *Appl. Catal. B Environ.* **2015**, *166–167*, 32–36. [[CrossRef](#)]
101. Baltrusaitis, J.; Jayaweera, P.M.; Grassian, V.H. Sulfur Dioxide Adsorption on TiO₂ Nanoparticles: Influence of Particle Size, Coadsorbates, Sample Pretreatment, and Light on Surface Speciation and Surface Coverage. *J. Phys. Chem. C* **2011**, *115*, 492–500. [[CrossRef](#)]
102. Langhammer, D.; Kullgren, J.; Österlund, L. Photoinduced Adsorption and Oxidation of SO₂ on Anatase TiO₂(101). *J. Am. Chem. Soc.* **2020**, *142*, 21767–21774. [[CrossRef](#)]
103. Mi, Y.; Weng, Y. Band Alignment and Controllable Electron Migration between Rutile and Anatase TiO₂. *Sci. Rep.* **2015**, *5*, 11482. [[CrossRef](#)] [[PubMed](#)]
104. Nosaka, Y.; Nosaka, A.Y. Reconsideration of Intrinsic Band Alignments within Anatase and Rutile TiO₂. *J. Phys. Chem. Lett.* **2016**, *7*, 431–434. [[CrossRef](#)] [[PubMed](#)]
105. Kaabeche, O.N.E.H.; Zouaghi, R.; Boukhedoua, S.; Bendjabeur, S.; Sehili, T. A Comparative Study on Photocatalytic Degradation of Pyridinium-Based Ionic Liquid by TiO₂ and ZnO in Aqueous Solution. *Int. J. Chem. React. Eng.* **2019**, *17*, 11482. [[CrossRef](#)]
106. Wojnárovits, L.; Takács, E. Rate Constants of Sulfate Radical Anion Reactions with Organic Molecules: A Review. *Chemosphere* **2019**, *220*, 1014–1032. [[CrossRef](#)]
107. Jayson, G.G.; Parsons, B.J.; Swallow, A.J. Some Simple, Highly Reactive, Inorganic Chlorine Derivatives in Aqueous Solution. *J. Chem. Soc. Faraday Trans. 1 Phys. Chem. Condens. Phases* **1973**, *69*, 1597–1607.
108. Maji, T.K.; Bagchi, D.; Kar, P.; Karmakar, D.; Pal, S.K. Enhanced Charge Separation through Modulation of Defect-State in Wide Band-Gap Semiconductor for Potential Photocatalysis Application: Ultrafast Spectroscopy and Computational Studies. *J. Photochem. Photobiol. A Chem.* **2017**, *332*, 391–398. [[CrossRef](#)]